J. Fluid Mech. (2024), *vol*. 984, A6, doi:10.1017/jfm.2024.154

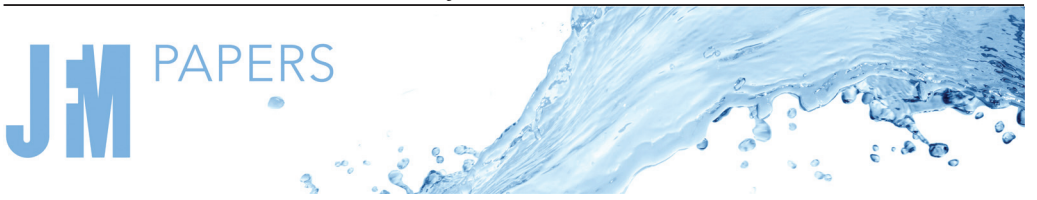

Large eddy simulation of flow over a circular cylinder with a neural-network-based subgrid-scale model

Myunghwa Kim[1], **Jonghwan Park**[1] **and Haecheon Choi**[1,2,†]

[1]Department of Mechanical Engineering, Seoul National University, Seoul 08826, Korea

[2]Institute of Advanced Machines and Design, Seoul National University, Seoul 08826, Korea

(Received 5 June 2023; revised 17 November 2023; accepted 14 February 2024)

A neural-network-based large eddy simulation is performed for flow over a circular cylinder. To predict the subgrid-scale (SGS) stresses, we train two fully connected neural network (FCNN) architectures with and without fusing information from two separate single-frame networks (FU and nFU, respectively), where the input variable is either the strain rate (SR) or the velocity gradient (VG). As the input variables, only the grid-filtered variables are considered for the SGS models of G-SR and G-VG, and both the grid- and test-filtered variables are considered for the SGS models of T-SR and T-VG. The training data are the filtered direct numerical simulation (fDNS) data at $Re_d = 3900$ based on the free-stream velocity and cylinder diameter. Using the same grid resolution as that of the training data, the performances of G-SR and G-VG (grid-filtered inputs) and T-SR-FU and T-VG-FU (grid- and test-filtered inputs with fusion) are better than those of the dynamic Smagorinsky model and T-SR-nFU and T-VG-nFU (grid- and test-filtered inputs without fusion). These FCNN-based SGS models are applied to untrained flows having different grid resolutions from that of training data. Although the performances of G-SR and G-VG are degraded, T-SR-FU and T-VG-FU still provide good performances. Finally, T-SR-FU and T-VG-FU trained at $Re_d = 3900$ are applied to higher-Reynolds-number flows ($Re_d = 5000$ and 10 000) and their results are also in good agreements with those of fDNS and previous experiment, indicating that adding the test-filtered variables and fusion increases the prediction capability even for untrained Reynolds number flows.

Key words: turbulence modelling, turbulence simulation, machine learning

† Email address for correspondence: choi@snu.ac.kr

1. Introduction

Large eddy simulation (LES) is an effective tool for accurately predicting turbulent flow by resolving large-scale eddies and modelling the effect of eddies smaller than the grid scale. Subgrid-scale (SGS) modelling finds a relation between the resolved flow variables and SGS stresses. So far, various SGS models have been proposed in a functional form based on turbulence theory and hypothesis. Many traditional SGS models adopt an eddy-viscosity approach based on the Boussinesq hypothesis (Smagorinsky 1963; Nicoud & Ducros 1999; Vreman 2004; Verstappen *et al.* 2010; Nicoud *et al.* 2011; Rozema *et al.* 2015; Trias *et al.* 2015; Silvis, Remmerswaal & Verstappen 2017). The eddy-viscosity model expresses a relation between the SGS stress tensor ($\boldsymbol{\tau}$) and filtered strain rate (SR) tensor ($\bar{\boldsymbol{S}}$) with a form of $\boldsymbol{\tau} - \frac{1}{3}\mathrm{tr}(\boldsymbol{\tau})\boldsymbol{I} = -2\nu_T\bar{\boldsymbol{S}}$, where $\boldsymbol{I}$ is the identity tensor, and ν_T is the eddy viscosity to be modelled with resolved flow variables. One of the most popular models based on the eddy-viscosity approach is the Smagorinsky model (Smagorinsky 1963), $\nu_T = (C_s\Delta)^2(2\bar{S}_{ij}\bar{S}_{ij})^{1/2}$, where C_s is a constant and Δ is the filter width. However, it is well known that the Smagorinsky model has a drawback in that a predetermined model coefficient C_s cannot handle various turbulent flows because it depends on the flow type, resolution, and local flow information. To overcome this drawback, the dynamic Smagorinsky model (DSM) (Germano *et al.* 1991) was developed, where the Smagorinsky model coefficient was dynamically determined by introducing a test filter (in addition to the grid filter) and Germano identity. Another type of SGS models is the similarity model (Bardina, Ferziger & Reynolds 1980; Liu, Meneveau & Katz 1994; Domaradzki & Saiki 1997), where the SGS stress tensor is assumed to be proportional to the resolved stress tensor $L_{ij}(= \widetilde{\overline{u_i}\,\overline{u_j}} - \widetilde{\overline{u_i}}\,\widetilde{\overline{u_j}})$. Here, the overbar and tilde denote two filtering operations, and the latter uses a wider filter width. In addition to these SGS models, other models such as the mixed model (Bardina *et al.* 1980; Zang, Street & Koseff 1993; Liu *et al.* 1994; Vreman, Geurts & Kuerten 1994; Liu, Meneveau & Katz 1995; Salvetti & Banerjee 1995; Horiuti 1997; Akhavan *et al.* 2000), gradient model (Clark, Ferziger & Reynolds 1979; Liu *et al.* 1994) and optimal model (Langford & Moser 1999; Völker, Moser & Venugopal 2002; Langford & Moser 2004; Zandonade, Langford & Moser 2004; Moser *et al.* 2009) have been also developed.

However, these traditional SGS models have some limitations. For example, the eddy viscosity models have low correlation coefficients between the actual and modelled SGS stresses even in *a priori* test (Clark *et al.* 1979; Liu *et al.* 1994). Moreover, the inverse energy transfer from the subgrid scales to the resolved ones (i.e. backscatter) cannot be predicted by this eddy viscosity model (Zang *et al.* 1993). This weakness can be overcome in DSM by dynamically determining the Smagorinsky model coefficient. However, the dynamic procedure may induce numerical instabilities in actual LES, and thus additional procedures like averaging in homogeneous directions or *ad hoc* clipping on negative eddy viscosity are required (Zang *et al.* 1993; Ghosal *et al.* 1995; Salvetti & Banerjee 1995; Lee, Choi & Park 2010). On the other hand, the scale-similarity model (SSM) provides relatively accurate backscatter and high correlation coefficients between the actual and modelled SGS stresses. However, when this model is applied to actual LES, dissipation is insufficient and simulations often diverge or inaccurately predict turbulence statistics (Bardina *et al.* 1980; Liu *et al.* 1994). Despite these limitations, the traditional SGS models still provide reasonable predictions for various turbulent flows, and many studies (Porté-Agel, Meneveau & Parlange 2000; Cui *et al.* 2004; Burton & Dahm 2005; Park *et al.* 2006; Lee *et al.* 2010; Rasthofer & Gravemeier 2013; Samiee, Akhavan-Safaei & Zayernouri 2020) have been conducted with this traditional approach to overcome the limitations mentioned above.

Recently, machine learning (ML) algorithms have been applied to the SGS modelling for LES as an another way to predict the SGS stresses using filtered flow variables. More specifically, fully connected neural network (FCNN, also called a multilayer perceptron; Gamahara & Hattori 2017; Zhou *et al.* 2019; Xie *et al.* 2020*a*; Xie, Wang & Weinan 2020*b*; Xie, Yuan & Wang 2020*c*; Yuan, Xie & Wang 2020; MacArt, Sirignano & Freund 2021; Park & Choi 2021; Subel *et al.* 2021; Wang *et al.* 2021; Kang, Jeon & You 2023), convolutional neural network (CNN; Beck, Flad & Munz 2019; Pawar *et al.* 2020; Zanna & Bolton 2020; Guan *et al.* 2022; Liu *et al.* 2022), and reinforcement learning (RL; Novati, de Laroussilhe & Koumoutsakos 2021; Kim *et al.* 2022; Kurz, Offenhäuser & Beck 2023) have been adopted. The FCNN is the simplest ML algorithm inspired by the biological neural networks that constitute animal brains. As the brains are trained by strengthening or weakening the synapses which are the connections between the nodes, the FCNN finds the optimised weight parameters which represent the connection strengths between the nodes to minimise a loss function such as the mean-square error. Many previous studies have adopted simple FCNN architectures which have two to six consecutive layers with many nodes. For instance, Wang *et al.* (2021) used two hidden layers and twenty nodes with invariants of the local velocity gradient (VG) tensor as inputs for forced incompressible isotropic turbulence. They showed that the FCNN-based LES was better than the traditional SGS models (DSM and dynamic mixed model [DMM]) both in trained and untrained (coarser than the trained) grid resolutions. Subel *et al.* (2021) applied an FCNN-based SGS model with six hidden layers with 250 nodes to a Burgers turbulence at untrained higher-Reynolds-number flows. Yuan *et al.* (2020) used an FCNN with four hidden layers and 128 or 64 nodes for forced incompressible isotropic turbulence, and showed that the FCNN-based LES outperformed the traditional SGS models such as DSM and DMM even for untrained filter widths. Park & Choi (2021) used an FCNN with two hidden layers and 128 nodes to predict the SGS stress for turbulent channel flow, and their FCNN-based SGS model performed better than DSM in actual LES, both for trained and untrained (grid resolution and Reynolds number) conditions. Meanwhile, Sirignano, MacArt & Freund (2020) and MacArt *et al.* (2021) adopted relatively complex FCNN architectures to predict isotropic turbulence and turbulent plane jet, respectively. As for more complex ML algorithms, people have suggested to use CNNs to learn flow structures even with fewer weight parameters than those of FCNNs. Pawar *et al.* (2020) compared the performances of FCNN- and CNN-based SGS models in a two-dimensional turbulence by conducting *a priori* test and showed that a CNN provided more accurate predictions than an FCNN did. However, they did not perform actual LES with the CNN. Liu *et al.* (2022) conducted actual LESs with both FCNN- and CNN-based SGS models for turbulent channel flow, and showed that, for untrained flow, a CNN-based SGS model performed well but LES with an FCNN-based SGS model diverged. Apart from SGS modelling, Font *et al.* (2021) developed a CNN-based closure model for the spanwise-averaged Navier–Stokes (SANS) equations, where the closure term of the SANS equations accounted for the three-dimensional effects that was not considered in two-dimensional formulations. They showed that this CNN-based closure model provided better predictions of flow over a circular cylinder than the two-dimensional formulations. On the other hand, RL can train the model with only limited target statistics, and training and simulation are carried out simultaneously in RL. For instance, Kim *et al.* (2022) proposed a physics-constrained deep RL for LES of turbulent channel flow for the purpose of finding an SGS model that maximises the statistical accuracy of turbulence quantities such as the mean viscous and Reynolds shear stresses. They showed that the results from the SGS models were in good agreements with the filtered DNS data. However, RL has a

difficulty for the prediction of turbulent flow over/inside a complex geometry, in that target statistics may not be available *a priori* for the complex flow.

For the simple flows such as isotropic turbulence and turbulent channel flow, FCNN-based SGS models have performed quite well even with a point-by-point learning process, which makes it possible to generalise the SGS models from one flow to another. Therefore, in the present study, we adopt an FCNN to construct an SGS model with a long-term goal of its application to flow over/inside a complex geometry. For the purpose of predicting such flow, various flow phenomena should be trained. The flow over a circular cylinder contains boundary layer development, flow separation, shear layer roll-up and turbulent wake. Therefore, the flow over a circular cylinder is a good starting point for constructing an FCNN-based SGS model for complex flows. The output variable from FCNN is the SGS stress tensor. As for the input variable, we consider the SR and VG tensors which provide good predictions for turbulent channel flow (Park & Choi 2021). The training data are the filtered flow variables from direct numerical simulation (DNS) of flow over a circular cylinder at $Re_d(= Ud/\nu) = 3900$, where U is the free-stream velocity, d is the cylinder diameter, and ν is the kinematic viscosity. With trained FCNNs, we perform *a priori* test and examine the prediction capability for the SGS shear stress, SGS dissipation and backscatter. In *a posteriori* test (actual LES), we perform LESs with FCNN-based SGS models at the trained flow condition, and compare the flow parameters, mean velocity and root-mean-square (r.m.s.) velocity fluctuations with those from filtered DNS, DSM and without SGS model. We finally conduct LESs with grid resolution and Reynolds numbers ($Re_d = 5000$ and 10 000) different from those of the trained condition, and discuss the prediction results. The details of the DNS and training data are given in § 2, and the training methods for the FCNN are described in § 3. The results of *a priori* and *a posteriori* tests for trained and untrained flows are given and discussed in § 4, followed by the conclusions in § 5.

2. Numerical details and training data

2.1. *Numerical details*

The governing equations for LES are the spatially filtered continuity and Navier–Stokes equations in the Cartesian coordinate using an immersed boundary method (Kim, Kim & Choi 2001),

$$\frac{\partial \bar{u}_i}{\partial x_i} - q = 0, \tag{2.1}$$

$$\frac{\partial \bar{u}_i}{\partial t} + \frac{\partial \bar{u}_i \bar{u}_j}{\partial x_j} = -\frac{\partial \bar{p}}{\partial x_i} + \frac{1}{Re_d}\frac{\partial^2 \bar{u}_i}{\partial x_j \partial x_j} - \frac{\partial \tau_{ij}}{\partial x_j} + f_i, \tag{2.2}$$

where $x_1\ (= x)$, $x_2\ (= y)$ and $x_3\ (= z)$ are the streamwise, transverse and spanwise directions, respectively, $u_i\ (= (u, v, w))$ are the corresponding velocity components, p is the pressure, t is time, $\tau_{ij}(= \overline{u_i u_j} - \bar{u}_i \bar{u}_j)$ is the SGS stress tensor, the overbar denotes the filtering operation and q and f_i are the mass source/sink and momentum forcing to satisfy the mass conservation and no-slip condition on the immersed boundary, respectively.

DNS of the flow over a circular cylinder is conducted at $Re_d = 3900$. The unfiltered continuity and Navier–Stokes equations ((2.1) and (2.2) with $\tau_{ij} = 0$) are solved using the second-order central difference scheme for all the spatial derivative terms on a staggered mesh, and a fractional step method with third-order Runge–Kutta and second-order Crank–Nicolson methods for the convection and diffusion terms, respectively. A computational domain and coordinate system are shown in figure 1(*a*), where the

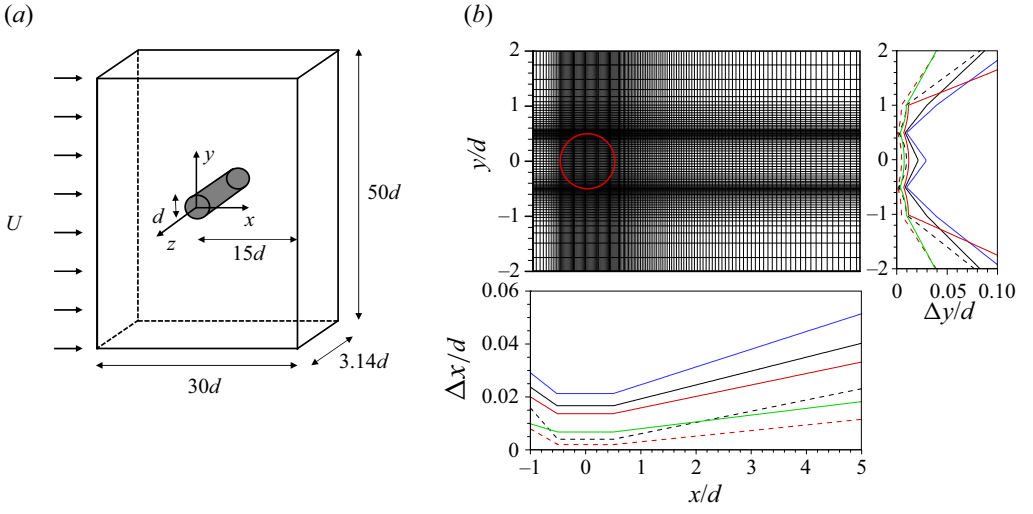

Figure 1. Computational domain, coordinate system and grid distributions for DNS and LES: (*a*) computational domain and coordinate system; (*b*) grid distributions near the circular cylinder. In (*b*), ---- (black), DNS3900; ---- (red), DNS5000; —— (black), LES3900; —— (blue), LES3900c; —— (red), LES3900f and LES5000; —— (green), LES10000.

cylinder centre is located at $(x, y) = (0, 0)$. The size of the computational domain is $L_x \times L_y \times L_z = 30d \times 50d \times 3.14d$. Note that this spanwise domain size has been adopted for DNS and LES by many previous studies (Beaudan & Moin 1994; Mittal 1995; Breuer 1998; Kravchenko & Moin 1998; Ma, Karamanos & Karniadakis 2000; Franke & Frank 2002; Dong *et al.* 2006; Park *et al.* 2006; Parnaudeau *et al.* 2008; Mani, Moin & Wang 2009; Lee 2010; Lehmkuhl *et al.* 2013; Li *et al.* 2020) and provides fully three-dimensional vortical structures in the wake (see, for example, figure 11). Moreover, the spanwise energy spectra fall off more than three decades at high spanwise wavenumbers (not shown here). A Dirichlet condition is used at the inlet, and a convective boundary condition, $\partial u_i/\partial t + c\partial u_i/\partial x = 0$, is used at the exit, where c is the plane-averaged streamwise velocity at the exit. The Neumann condition ($\partial u/\partial y = \partial w/\partial y = 0, v = 0$) is used at the far-field boundary, and the periodic condition is imposed in the spanwise direction. A no-slip boundary condition on the cylinder surface is satisfied with an immersed boundary method (Kim *et al.* 2001). The number of grid points for DNS is $N_x \times N_y \times N_z = 1025 \times 501 \times 128$. The grids are uniformly distributed in z direction ($\Delta z = 0.02453d$) and non-uniformly distributed in x and y directions, respectively, and they are densely allocated near the cylinder surface and separating shear layer region (figure 1*b*): e.g. the smallest grid sizes are $\Delta x_{min} = 0.004d$ and $\Delta y_{min} = 0.002d$, respectively.

The data from the present DNS are validated by comparing them with those from the previous experiment (Parnaudeau *et al.* 2008) and DNS (Ma *et al.* 2000). Figure 2 shows the transverse profiles of the mean streamwise velocity and r.m.s. streamwise velocity fluctuations at three streamwise locations in the wake ($x/d = 1.06$, 1.54 and 2.02), respectively. As shown, the present results are in excellent agreements with those of previous experiment and DNS, indicating that the choices of grids and computational domain for DNS are appropriate.

To estimate the prediction capabilities of the FCNN-based SGS models at untrained Reynolds numbers, another DNS is performed at $Re_d = 5000$. The computational domain size and boundary conditions are the same as those of $Re_d = 3900$, as described previously. We consider three different grid distributions for the convergence of solution:

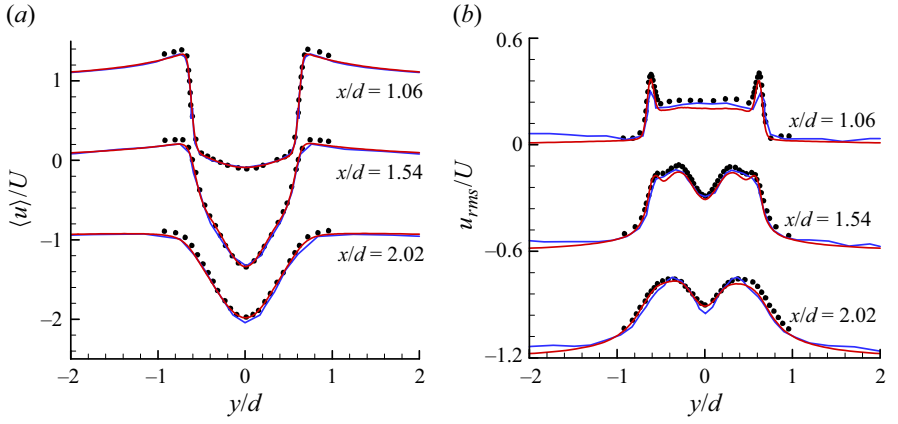

Figure 2. Turbulence statistics from DNS ($Re_d = 3900$): (*a*) mean streamwise velocity; (*b*) r.m.s. streamwise velocity fluctuations. —— (red), Present DNS; •, experiment (Parnaudeau *et al.* 2008); —— (blue), DNS (Ma *et al.* 2000). Here, the bracket $\langle\cdot\rangle$ denotes the averaging over the spanwise direction and in time.

Cases	(N_x, N_y, N_z)	$(\Delta x_{min}/d, \Delta y_{min}/d)$	L_r/d	$\langle C_{pb}\rangle$	U_{min}/U	$\langle C_D\rangle$
Present DNS	(2049, 1001, 128)	(0.002, 0.001)	1.39	−0.91	−0.30	1.01
	(2049, 1001, 192)	(0.002, 0.001)	1.41	−0.89	−0.29	1.00
	(3073, 1281, 128)	(0.00133, 0.0008)	1.37	−0.91	−0.33	1.01
Experiment	—	—	1.40[c]	−0.93[b]	−0.45[c]	1.02[a]
DNS[d]	—	—	1.14	−1.02	−0.24	1.12

Table 1. Flow quantities at $Re_d = 5000$ from present DNSs, together with those from previous experiments and DNS. Here, L_r is the mean recirculation length measured from the base point of the cylinder, $\langle C_{pb}\rangle$ is the mean base pressure coefficient, U_{min} is the maximum mean negative velocity along the centreline and $\langle C_D\rangle$ is the mean drag coefficient.

[a]Norberg (1993).
[b]Norberg (1994).
[c]Norberg (1998).
[d]Aljure *et al.* (2017).

$(N_x, N_y, N_z) = (2049, 1001, 128)$, $(2049, 1001, 192)$ and $(3073, 1281, 128)$, respectively. The second simulation has 1.5 times as many grid points in the spanwise direction as the first, and the third simulation uses about 1.5 times and 1.3 times as many grid points in x and y directions as the first, respectively (see table 1). The results from these three simulations at $Re_d = 5000$ are compared with those from previous experiment and DNS in table 1 and figure 3. As shown, the results from three simulations are very similar among themselves, demonstrating the grid convergence of the present DNS. Although the mean streamwise velocity and r.m.s. streamwise velocity fluctuations along the centreline from the DNSs and experiment show some differences at $x/d < 2$ (within recirculation zone), they overall agree very well with those from the previous experiments (Norberg 1993, 1994, 1998), validating the accuracy of the present DNS.

LESs of turbulent flow over a circular cylinder are performed at $Re_d = 3900$, 5000 and 10 000, respectively, with the FCNN-based SGS models developed during the present study and DSM. Numerical methods for solving the filtered continuity and Navier–Stokes equations ((2.1) and (2.2)) are the same as those of DNS. The second-order finite difference method applied to all the spatial derivative terms on a staggered mesh conserves kinetic

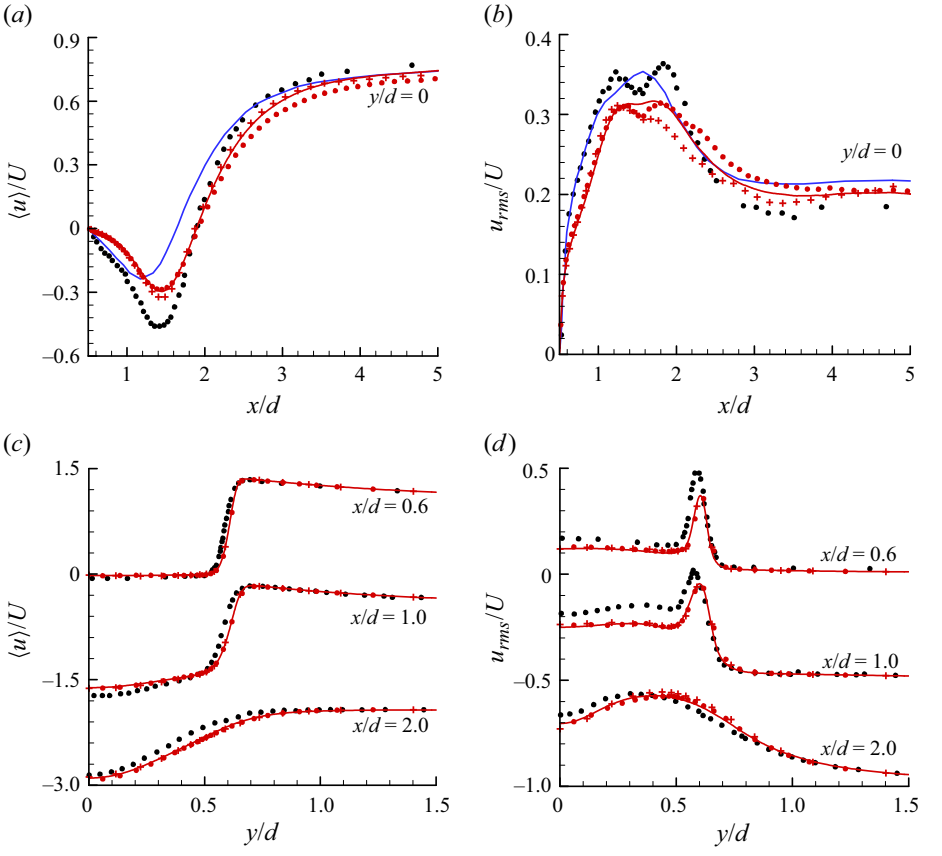

Figure 3. Turbulence statistics from present DNSs ($Re_d = 5000$): (*a*) mean streamwise velocity along the centreline; (*b*) r.m.s. streamwise velocity fluctuations along the centreline; (*c*) mean streamwise velocity in the wake; (*d*) r.m.s. streamwise velocity fluctuations in the wake. Present DNSs (—— (red), $N_x \times N_y \times N_z = 2049 \times 1001 \times 128$; • (red), $2049 \times 1001 \times 192$; + (red), $3073 \times 1281 \times 128$); • (black), experiment (Norberg 1998); —— (blue), DNS (Aljure *et al.* 2017).

energy as well as continuity and momentum, and does not exhibit numerical dissipation. These features make the scheme suitable for use in LES, and various complex flows have been successfully simulated using it (Mittal & Moin 1997). During simulation, kinetic energy is dissipated by viscous and SGS dissipation. LES without SGS dissipation can be stable when viscous dissipation alone is sufficient to maintain stability, but provides an inaccurate result. However, it becomes unstable on very coarse grids due to lack of dissipation. For DSM, a box filter of $\tilde{\Delta}_z = 2\bar{\Delta}_z$ is used as the test filter, where $\bar{\Delta}_z$ is the grid size in the homogeneous direction (z). The domain size for LES is the same as that for DNS, but the number of grid points for LES at $Re_d = 3900$ is $N_x \times N_y \times N_z = 449 \times 271 \times 64$ (same number of grid points used in Lee 2010) whose resolution is the same as that of training data. We also conduct LESs with coarser and finer grid resolutions at $Re_d = 3900$, respectively. For $Re_d = 5000$ and 10 000, we use finer grid resolutions (see table 3 later in this paper). The present computations are performed at the computational time steps of $\Delta tU/d = 0.004$, 0.003 and 0.0025 for $Re_d = 3900$, 5000 and 10 000, respectively. After reaching a statistically equilibrium state, the turbulence statistics at these Reynolds numbers are obtained by averaging over $TU/d = 200$, 150 and 125, respectively.

2.2. *Training data*

As shown in Park & Choi (2021), an FCNN trained with two databases obtained from two different grid sets predicted turbulent channel flow in LES better than an FCNN trained with a database obtained from one grid set, when LES is performed with a grid set different from those used for training. In the present study, we do not pursue the same approach as done in Park & Choi (2021). We rather construct a database obtained with a grid set, apply a test filter having a wider filter width to it to create another database having coarser grid resolution, and train an FCNN with these two databases. Using this approach, one can certainly reduce the effort of constructing databases for training. As shown later (§ 4.2), this approach successfully predicts the flow over a circular cylinder even if the grid distribution is different from that used for training. In Appendix D, we also show the result for turbulent channel flow.

Let us apply two filters ($\bar{G}$ and $\tilde{G}$, called grid and test filters, respectively) to a flow variable (f) obtained by DNS, and calculate two filtered DNS (fDNS) variables ($\bar{f}$ and $\tilde{f}$) as follows:

$$\bar{f}(x) = \int f(x')\bar{G}(x, x')\,\mathrm{d}x', \tag{2.3}$$

$$\tilde{f}(x) = \int f(x')\tilde{G}(x, x')\,\mathrm{d}x', \tag{2.4}$$

where $G(x, x')$ and $\tilde{G}(x, x')$ are box filter kernels, a type of filter applicable to flow over a complex geometry. With the box filter applied in all the (x, y, z) directions, the grid-filtered flow variable $\bar{f}$ is obtained as

$$\bar{f}(x, y, z, t) = \frac{1}{\bar{\Delta}_x\bar{\Delta}_y\bar{\Delta}_z}\int_{-0.5\bar{\Delta}_z}^{0.5\bar{\Delta}_z}\int_{-0.5\bar{\Delta}_y}^{0.5\bar{\Delta}_y}\int_{-0.5\bar{\Delta}_x}^{0.5\bar{\Delta}_x} f(x+x', y+y', z+z', t)\,\mathrm{d}x'\,\mathrm{d}y'\,\mathrm{d}z', \tag{2.5}$$

where $\bar{\Delta}_i$ (the grid size of LES) is the filter size in i direction. A one-sided box filter is used near the cylinder surface. The test-filtered flow variable $\tilde{\bar{f}}$ is obtained by applying the box filter (applied only in the spanwise direction) to the grid-filtered variable $\bar{f}$ as

$$\tilde{\bar{f}}(x, y, z, t) = \frac{1}{\tilde{\Delta}_z}\int_{-0.5\tilde{\Delta}_z}^{0.5\tilde{\Delta}_z}\bar{f}(x, y, z+z', t)\,\mathrm{d}z', \tag{2.6}$$

where $\tilde{\Delta}_z(>\bar{\Delta}_z)$ is the size of test filter in z direction. With the operations of (2.5) and (2.6), training data (i.e. grid- and test-fDNS data) are obtained. The training data are extracted from 25 instantaneous fDNS fields during approximately 20 vortex shedding cycles ($TU/d \approx 100$; see figure 4*a*). Adding more instantaneous fDNS fields does not improve the prediction performance (see Appendix A for the details). From each instantaneous flow field, the fDNS data on (x, y) planes at four different spanwise locations (only 278×158 grid points per plane within a dashed box in figure 4*b*) are taken as the training data to filter out highly correlated data. Thus, the total number of training data is $N_{tot} = 25 \times N_{xy} \times 4 = 4\,078\,400$, where $N_{xy}(= 40\,784)$ is the number of grid points within the dashed box except for those inside a circular cylinder. The region close to the cylinder surface denoted as the dashed box ($-1 \le x/d \le 6$ and $-1.5 \le y/d \le 1.5$) contains laminar and turbulent flows, and the representative flow phenomena such as the boundary layer development, flow separation, shear layer roll-up and turbulent wake. We also increase the size of the dashed box to $-1 \le x/d \le 8$ and $-2 \le y/d \le 2$, but

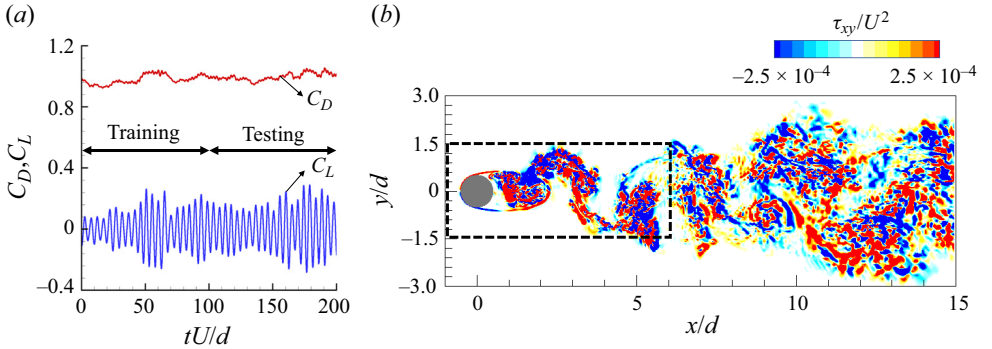

Figure 4. Spatiotemporal extraction of the training data: (*a*) time histories of the drag and lift coefficients (DNS); (*b*) contours of the instantaneous SGS shear stress τ_{xy}. In (*b*), the dashed box denotes the (x, y) plane where training data are extracted.

Cases	Fusion	Input variable(s)	Number of input components (N_q)
G-SR	—	$\bar{S}_{ij}$	6
G-VG	—	$\bar{\alpha}_{ij}$	9
T-SR-nFU	X	$\bar{S}_{ij}$ and $\tilde{\bar{S}}_{ij}$	12
T-VG-nFU	X	$\bar{\alpha}_{ij}$ and $\tilde{\bar{\alpha}}_{ij}$	18
T-SR-FU	O	$\bar{S}_{ij}$ and $\tilde{\bar{S}}_{ij}$	12
T-VG-FU	O	$\bar{\alpha}_{ij}$ and $\tilde{\bar{\alpha}}_{ij}$	18

Table 2. Model architectures and input variables for NNs.

a posteriori test provides only few changes in the LES results (see Appendix A for the details).

3. FCNN training

3.1. *Input and output variables*

The present FCNNs (denoted as NNs hereafter) use four different input variables to predict the six components of the SGS stress tensor τ_{ij}, as listed in table 2. The grid-filtered variables are used as inputs for all NNs, whereas the test-filtered variables are used as inputs only for the cases of T-SR and T-VG. The input variables for the cases of G-SR and G-VG are the six components of the SR tensor ($\bar{S}_{ij} = 0.5(\partial\bar{u}_i/\partial x_j + \partial\bar{u}_j/\partial x_i)$) and nine components of the VG tensor ($\bar{\alpha}_{ij} = \partial\bar{u}_i/\partial x_j$) at each input grid point, respectively, and the output variable is the six components of τ_{ij} at the same grid point. The choice of these input variables comes from the previous NN-based LES of turbulent channel flow by Park & Choi (2021), in which the SGS models with the inputs of $\bar{S}_{ij}$ and $\bar{\alpha}_{ij}$ were used and provided good prediction performances.

For the cases of T-SR and T-VG, both the grid- and test-filtered variables are used as the input variables. The use of test-filtered variables or similar as an input to NN is not the first time. Xie *et al.* (2020*a*) used the first-order derivatives of the grid- and test-filtered velocity and temperature at multiple grid points as inputs for compressible isotropic turbulence, and showed that their predictions of the velocity and temperature spectra were better than those by the DMM. Park & Choi (2021) trained an NN with input variables from

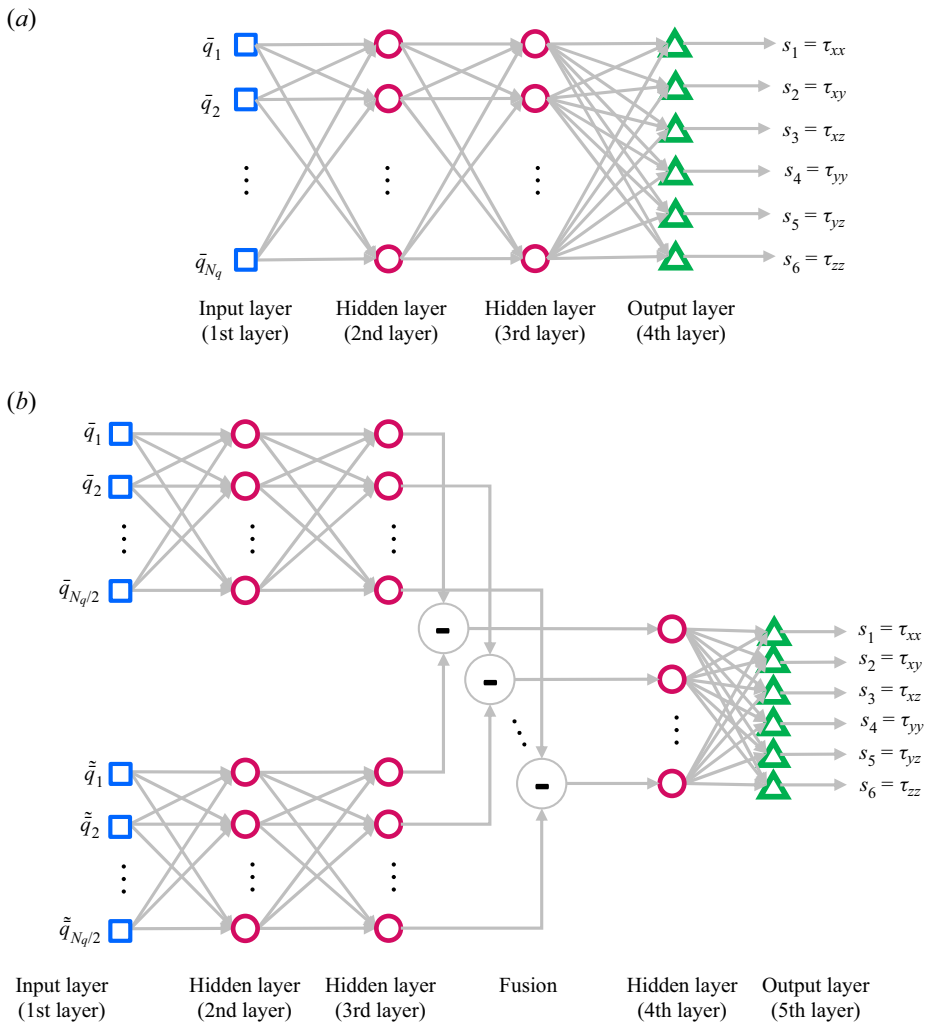

Figure 5. Schematic diagrams of the present NNs: (*a*) NN with two hidden layers (denoted as nFU architecture); (*b*) NN with two and one hidden layers before and after fusion (subtraction), respectively (denoted as FU architecture). Here, $\bar{\boldsymbol{q}}$ and $\tilde{\bar{\boldsymbol{q}}}$ are the grid- and test-filtered inputs, respectively, N_q is the number of input components (see table 2), and $\boldsymbol{s}$ is the output.

fDNS datasets obtained from two different filter widths, and showed that its prediction for turbulent channel flow was better than that from single fDNS dataset when an actual LES was performed with a grid resolution different from that used for training. Therefore, the addition of the test-filtered variables to the input should enhance the prediction capability of NN-based SGS models, especially when the grid resolution for LES is different from that used for training.

3.2. *Neural network architectures*

Most of the previous studies have adopted simple NN architectures having consecutive layers with multiple nodes (see, for example, Sarghini, de Felice & Santini 2003; Wollblad & Davidson 2008; Gamahara & Hattori 2017; Pal 2019; Xie *et al.* 2020*a*,*b*,*c*; Yuan *et al.* 2020; Park & Choi 2021; Stoffer *et al.* 2021; Subel *et al.* 2021; Wang *et al.* 2021; Kang *et al.* 2023), as shown in figure 5(*a*). Park & Choi (2021) used an NN with two hidden

layers and 128 nodes per hidden layer by setting $\bar{S}_{ij}$ or $\bar{\alpha}_{ij}$ as the input and τ_{ij} as the output, respectively, and showed its better performance than that of DSM for turbulent channel flow. However, when the grid resolution of LES was different from that of training data, the trained SGS model could not accurately predict turbulence statistics. This problem was overcome by training an SGS model with data obtained from multiple filter widths, but its performance can be degraded when the grid sizes used for LES are out of the range of training grid sizes. We use the same NN architecture (denoted as nFU architecture), and test for the present flow over a circular cylinder with grid resolutions different from the training one, resulting in similar degradation of the prediction performance (see § 4.2.2). We also increase the numbers of the hidden layers and nodes to 3 and 256, respectively, but these increases do not improve the prediction performances (see Appendix B for the details).

Karpathy *et al.* (2014) suggested three types of fusion (early fusion, late fusion and slow fusion) to classify a video having spatiotemporal features. In that study, with shared CNN parameters, spatial features from multiple contiguous frames in time were extracted, and then the extracted features were combined by fusion. Analogous to the video classification, one may construct an NN architecture by combining extracted features from inputs with different grid resolutions by fusion. Motivated by this approach, we build a new NN architecture (denoted as FU architecture; figure 5*b*) by introducing additional test-filtered variables and fusing information from two separate single-frame networks. Among the three types of fusion, we adopt late fusion to consider not only the grid- and test-filtered input variables but also their difference. The present FU architecture consists of two and one hidden layers before and after fusion, respectively, and 64 nodes per hidden layer (see § 3.3). This fusion process is also motivated by the dynamic procedure of DSM (Germano *et al.* 1991; Lilly 1992). In DSM, the SGS stresses at the grid and test filter levels, τ_{ij} and T_{ij}, are parameterised with the same functional form, and the resolved turbulent stress, $\mathcal{L}_{ij} = T_{ij} - \tilde{\tau}_{ij}$, is calculated explicitly. The resolved turbulent stress represents the contribution to the Reynolds stress from the length scales between the grid and test filter widths. Therefore, we expect that fusion in the FU architecture should be able to properly treat the resolved turbulent stress from the grid- and test-filtered variables, and thus enable to produce more accurate SGS stresses.

3.3. *Training details*

In the nFU architecture (no fusion), the output of the mth layer, $\boldsymbol{h}^{(m)}$, is given as

$$\left.\begin{aligned}
h_i^{(1)} &= \overline{q_i} \quad (i = 1, 2, \ldots, N_q); \\
h_j^{(2)} &= \max\left[0, \gamma_j^{(2)} \left(\sum_{i=1}^{N_q} W_{ij}^{(1)(2)} h_i^{(1)} + b_j^{(2)} - \mu_j^{(2)}\right) \Big/ \sigma_j^{(2)} + \beta_j^{(2)}\right] \\
&\quad (j = 1, 2, \ldots, 128); \\
h_k^{(3)} &= \max\left[0, \gamma_k^{(3)} \left(\sum_{j=1}^{128} W_{jk}^{(2)(3)} h_j^{(2)} + b_k^{(3)} - \mu_k^{(3)}\right) \Big/ \sigma_k^{(3)} + \beta_k^{(3)}\right] \\
&\quad (k = 1, 2, \ldots, 128); \\
h_l^{(4)} &= s_l = \sum_{k=1}^{128} W_{kl}^{(3)(4)} h_k^{(3)} + b_l^{(4)} \quad (l = 1, 2, \ldots, 6),
\end{aligned}\right\} \tag{3.1}$$

where $\bar{\boldsymbol{q}}$ is the grid-filtered input, N_q is the number of the inputs, $\boldsymbol{W}^{(m)(m+1)}$ is the weight matrix between mth and $(m+1)$th layers, $\boldsymbol{b}^{(m)}$ is the bias of the mth layer, $\boldsymbol{s}$ is the output and $\boldsymbol{\mu}^{(m)}$, $\boldsymbol{\sigma}^{(m)}$, $\boldsymbol{\gamma}^{(m)}$ and $\boldsymbol{\beta}^{(m)}$ are the parameters for a batch normalisation (Ioffe & Szegedy 2015). A rectified linear unit (ReLu; Nair & Hinton 2010) is used as an activation function, and mean-squared error (MSE) is used as a loss function defined as

$$L = \frac{1}{2N_{xy}} \frac{1}{6} \sum_{l=1}^{6} \sum_{n=1}^{N_{xy}} \left(s_{l,n}^{\mathrm{fDNS}} - s_{l,n} \right)^2, \tag{3.2}$$

where $\boldsymbol{s}^{\mathrm{fDNS}}$ is the SGS stress tensor obtained from fDNS data, and $N_{xy}(= 40\,784$; see § 2.2) is the size of the batch.

Similarly, in the FU architecture (with fusion), the output of the mth layer, $\boldsymbol{h}^{(m)}$, is as follows:

$$\left.\begin{aligned}
&h_{1i}^{(1)} = \overline{q_i} \quad (i = 1, 2, \ldots, N_q/2);\\
&h_{2i}^{(1)} = \widetilde{\overline{q_i}} \quad (i = 1, 2, \ldots, N_q/2);\\
&h_{1j}^{(2)} = \max\left[0, \gamma_{1j}^{(2)} \left(\sum_{i=1}^{N_q/2} W_{1ij}^{(1)(2)} h_{1i}^{(1)} + b_{1j}^{(2)} - \mu_{1j}^{(2)} \right) \Big/ \sigma_{1j}^{(2)} + \beta_{1j}^{(2)} \right]\\
&\qquad (j = 1, 2, \ldots, 64);\\
&h_{2j}^{(2)} = \max\left[0, \gamma_{2j}^{(2)} \left(\sum_{i=1}^{N_q/2} W_{2ij}^{(1)(2)} h_{2i}^{(1)} + b_{2j}^{(2)} - \mu_{2j}^{(2)} \right) \Big/ \sigma_{2j}^{(2)} + \beta_{2j}^{(2)} \right]\\
&\qquad (j = 1, 2, \ldots, 64);\\
&h_{1k}^{(3)} = \max\left[0, \gamma_{1k}^{(3)} \left(\sum_{j=1}^{64} W_{1jk}^{(2)(3)} h_{1j}^{(2)} + b_{1k}^{(3)} - \mu_{1k}^{(3)} \right) \Big/ \sigma_{1k}^{(3)} + \beta_{1k}^{(3)} \right]\\
&\qquad (k = 1, 2, \ldots, 64);\\
&h_{2k}^{(3)} = \max\left[0, \gamma_{2k}^{(3)} \left(\sum_{j=1}^{64} W_{2jk}^{(2)(3)} h_{2j}^{(2)} + b_{2k}^{(3)} - \mu_{2k}^{(3)} \right) \Big/ \sigma_{2k}^{(3)} + \beta_{2k}^{(3)} \right]\\
&\qquad (k = 1, 2, \ldots, 64);\\
&h_{k}^{(4)} = h_{1k}^{(3)} - h_{2k}^{(3)} \quad (k = 1, 2, \ldots, 64);\\
&h_{l}^{(5)} = s_l = \sum_{k=1}^{64} W_{kl}^{(4)(5)} h_{k}^{(4)} + b_{l}^{(5)} \quad (l = 1, 2, \ldots, 6),
\end{aligned}\right\} \tag{3.3}$$

where $\bar{\boldsymbol{q}}$ and $\tilde{\bar{\boldsymbol{q}}}$ are the grid- and test-filtered inputs, respectively, $\boldsymbol{h}^{(4)}$ is from fusion (Karpathy *et al.* 2014), and other parameters are the same as those in the nFU architecture. A stochastic gradient descent with a learning rate of 0.01 is used to optimise the trainable parameters, and the weight and bias are initialised by using Xavier (Glorot & Bengio 2010) and zero initialisations, respectively. Training and validation data are extracted from 25 and 7 instantaneous fields, respectively (approximately 75 % of instantaneous fields for training and 25 % for validation). With these databases, the NNs are trained, and training is

stopped to avoid overfitting if the validation loss increases. Both nFU and FU architectures are trained by using the Python open-source library, TensorFlow.

While training the NNs, the input and output variables are normalised by the free-stream velocity U and cylinder diameter d. In turbulent channel flow, Park & Choi (2021) used the input and output variables in wall units, and showed that the SGS model has an excellent prediction performance not only at the trained Reynolds number but also at a higher Reynolds number when the grid resolutions in wall units are the same. However, for the present flow, the wall unit is not proper for normalisation because it contains turbulent wake behind the cylinder surface. We also consider the normalisation of flow variables with the mean and r.m.s. values, such as $\tau_{ij}^{*}(x, y, z, t) = (\tau_{ij}(x, y, z, t) - \tau_{ij}^{mean}(x, y))/\tau_{ij}^{rms}(x, y)$, to scale the input and output variables with zero mean and unit variance. Although this normalisation may be good for training the architecture, it requires *a priori* knowledge about the mean and r.m.s. values for untrained Reynolds number flow. Thus, we normalise the input and output variables with U and d.

4. Results

In § 4.1, we perform *a priori* tests at $Re_d = 3900$ and 5000 with the nFU and FU architectures that are trained with the fDNS data at $Re_d = 3900$. The SGS shear stress, SGS dissipation and backward SGS dissipation obtained by the trained architectures are compared with those of fDNS and DSM. In § 4.2.1, *a posteriori* tests (i.e. actual LESs) are conducted at $Re_d = 3900$ with the same grid resolution as that of the trained fDNS data. These LES results are compared with those of fDNS and from LESs with DSM and without SGS model, respectively. In § 4.2.2, we perform LESs at $Re_d = 3900$ with grid resolutions different from that of the trained fDNS data, and discuss the results. Finally, in § 4.2.3, LESs are carried out at $Re_d = 5000$ and 10 000, and their results are compared with those of fDNS and previous experiment.

4.1. *A priori tests*

A priori tests at $Re_d = 3900$ and 5000 are conducted with the nFU and FU architectures trained at $Re_d = 3900$. We do not conduct *a priori* test for $Re_d = 10\,000$, because the fDNS data at this Reynolds number are not available at hand. Figure 6 shows the profiles of the mean SGS shear stress $\langle\tau_{xy}\rangle$, mean SGS dissipation $\langle\epsilon_{SGS}\rangle$ and mean backward SGS dissipation $\langle\epsilon_{SGS}^{-}\rangle$ (backscatter) at $x/d = 1.06$, 1.54 and 2.02 for $Re_d = 3900$ and 5000, respectively, where $\epsilon_{SGS} = -\tau_{ij}\bar{S}_{ij}$ and $\langle\epsilon_{SGS}^{-}\rangle = \frac{1}{2}\langle\epsilon_{SGS} - |\epsilon_{SGS}|\rangle$. Also shown in figure 6 are those of fDNS and from DSM.

At $x/d = 1.06$, G-SR and G-VG, and T-SR-FU and T-VG-FU, respectively, show similar predictions of $\langle\tau_{xy}\rangle$ and $\langle\epsilon_{SGS}\rangle$. However, the SGS shear stresses from T-SR-nFU and T-VG-nFU have negative and positive peaks in the lower and upper shear layer regions for $Re_d = 3900$, respectively, which is opposite to that of fDNS data. A similar behaviour is observed for the SGS dissipation. The backscatter profiles ($\langle\epsilon_{SGS}^{-}\rangle$) from G-SR, G-VG, T-SR-nFU and T-VG-nFU contain high peaks in the upper and lower shear layer regions unlike that of fDNS data, but those from T-SR-FU and T-VG-FU are underpredicted but similar to that of fDNS. On the other hand, at $x/d = 1.54$ and 2.02, G-SR, T-SR-nFU and T-SR-FU (input of $\bar{S}_{ij}$), and G-VG, T-VG-nFU and T-VG-FU (input of $\bar{\alpha}_{ij}$) show similar performances, respectively, regardless of using fusion. The predictions from all the architectures are better than that from DSM (note that the backscatter from DSM is zero). The architectures with the input of $\bar{\alpha}_{ij}$ predict these statistics better than those with the input of $\bar{S}_{ij}$. However, as is well known from the studies of the traditional and NN-based

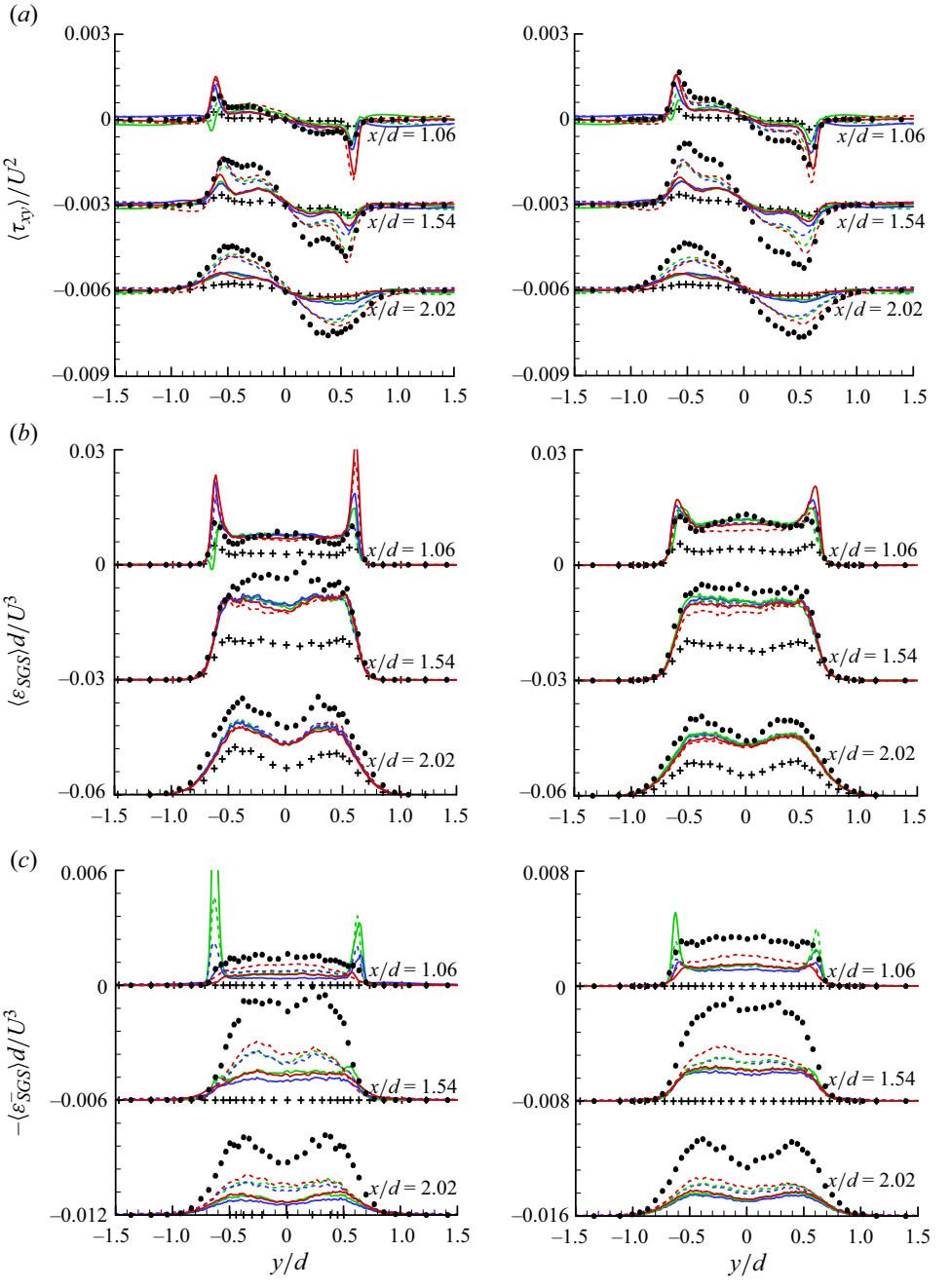

Figure 6. Statistics of the SGS variables at three streamwise locations in the wake from *a priori* tests ($Re_d = 3900$ (left) and 5000 (right)): (*a*) mean SGS shear stress $\langle\tau_{xy}\rangle$; (*b*) mean SGS dissipation $\langle\epsilon_{SGS}\rangle$; (*c*) mean backscatter $\langle\bar{\epsilon}_{SGS}\rangle$. •, fDNS; —— (blue), G-SR; ---- (blue), G-VG; —— (green), T-SR-nFU; ---- (green), T-VG-nFU; —— (red), T-SR-FU; ---- (red), T-VG-FU; +, DSM.

SGS modelling (Park *et al.* 2006; Gamahara & Hattori 2017; Beck *et al.* 2019; Park & Choi 2021), a better prediction in *a priori* test does not guarantee a better performance in *a posteriori* test (i.e. actual LES).

As discussed in Duraisamy (2021), one of the reasons for this inconsistency between *a priori* and *a posteriori* tests is that errors are accumulated over time and, thus, resolved scales are corrupted. Hence, we take another *a priori* test to assess the robustness of the NN-based SGS models. The robustness is one of the indices that can represent the sensitivity of the NNs, defined as the degree to which a system or component can function correctly in the presence of invalid inputs or stressful environmental conditions (IEEE 1990). Thus, we add noise to the present inputs ($\bar{S}_{ij}$ and $\tilde{\bar{S}}_{ij}$) and observe how outputs (τ_{ij}) are changed for the present NN-based SGS models. Let us define $\bar{\sigma}_{ij}$ and $\tilde{\bar{\sigma}}_{ij}$ as the standard deviations of the inputs ($\bar{S}_{ij}$ and $\tilde{\bar{S}}_{ij}$) in the training databases, respectively. Then, the random inputs are added as follows (Ferri, Hernández-Orallo & Modroiu 2009; Fabra-Boluda *et al.* 2022):

$$\left.\begin{aligned} \bar{S}'_{ij} &= \bar{S}_{ij} + N(0, \bar{\sigma}_{ij}^2), \\ \tilde{\bar{S}}'_{ij} &= \tilde{\bar{S}}_{ij} + N(0, \tilde{\bar{\sigma}}_{ij}^2), \end{aligned}\right\} \tag{4.1}$$

where $N(0, \sigma^2)$ is the normal distribution with zero mean and standard deviation of σ. We consider G-SR, T-SR-nFU and T-SR-FU for assessing their robustness, and results are shown in figure 7. The changes in the normal and shear SGS stresses (τ_{xx}, τ_{yy} and τ_{xy}) are bigger for G-SR and T-SR-nFU than those for T-SR-FU, whereas the changes in τ_{zz} are relatively insensitive to the models except the shear layer region at $x/d = 1.06$ for T-SR-nFU. This result indicates that T-SR-FU is the most robust among these models. Therefore, we expect better performance from *a posteriori* test with T-SR-FU (see the following).

4.2. *A posteriori tests*

A posteriori tests (actual LESs) are conducted for flow over a circular cylinder at $Re_d = 3900$, 5000 and 10 000 with the NN-based SGS models trained at $Re_d = 3900$. The computational domain size is fixed to be $30d \times 50d \times 3.14d$ for all cases. Table 3 summarises the computational parameters for LESs and flow parameters obtained from LESs with various SGS models, together with those of DNS, DSM and no SGS model. Note that, in LES with DSM, the model coefficient of the eddy viscosity is obtained by averaging over z direction (Germano *et al.* 1991; Lilly 1992; Mittal & Moin 1997; Breuer 1998; Kravchenko & Moin 2000; Mani *et al.* 2009). The grid resolution for the cases of LES3900 is the same as that of fDNS used in training SGS models, and those of LES3900c and LES3900f are coarser and finer than that of LES3900, respectively. In cases of LES5000 and LES10000, the grid resolutions are finer than that of LES3900. For $Re_d = 5000$, the numbers of grid points used for DNS and fDNS are $2049 \times 1001 \times 128$ and $545 \times 301 \times 64$, respectively, and the grid resolution for the cases of LES5000 is the same as that of fDNS. More on the grid-resolution study for *a posteriori* tests at $Re_d = 3900$, 5000 and 10 000 is given in Appendix C.

4.2.1. *LES with the grid resolution same as that of training data ($Re_d = 3900$)*

As listed in table 3, for LES3900, the statistics from G-SR and G-VG and T-SR-FU and T-VG-FU are in good agreements with those of DNS, whereas T-SR-nFU and T-VG-nFU

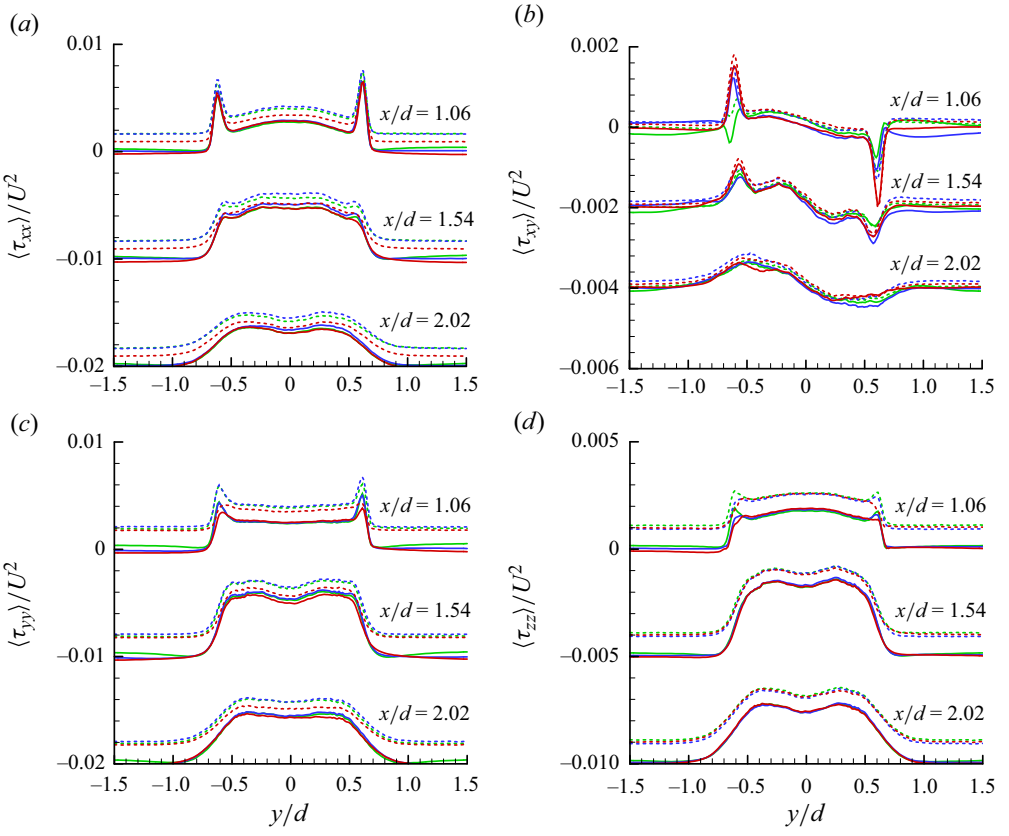

Figure 7. Robustness of the NN-based SGS models under the inputs without and with noise (equation 4.1) ($Re_d = 3900$): (*a*) $\langle\tau_{xx}\rangle$; (*b*) $\langle\tau_{xy}\rangle$; (*c*) $\langle\tau_{yy}\rangle$; (*d*) $\langle\tau_{zz}\rangle$. —— (blue), G-SR without noise; ---- (blue), G-SR with noise; —— (green), T-SR-nFU without noise; ---- (green), T-SR-nFU with noise; —— (red), T-SR-FU without noise; ---- (red), T-SR-FU with noise.

do not predict these statistics very well. In particular, G-SR, G-VG, T-SR-FU and T-VG-FU predict the recirculation length and base pressure coefficient more accurately than DSM does. The profiles of the mean streamwise velocity and r.m.s. streamwise velocity fluctuations at three streamwise locations in the wake from LES3900 are shown in figure 8, together with those of fDNS, DSM and no SGS model. As shown, the results from G-SR, G-VG, T-SR-FU and T-VG-FU are in excellent agreements with those of fDNS and are better than those of DSM, whereas T-SR-nFU and T-VG-nFU show poor predictions (T-SR-nFU is even worse than no SGS model). Figure 9 shows the contours of the instantaneous vorticity magnitude at a spanwise location from the present SGS models, fDNS, DSM and no SGS model, respectively. At $Re_d = 3900$, the upper and lower shear layers are elongated downstream and very few vortical structures exist very near the base surface (see the case of fDNS in this figure). However, the contours from no SGS model are significantly distorted in the shear layer and near-wake contains full of small scales because of lack of turbulent dissipation. The cases of T-SR-nFU and T-VG-nFU show somewhat similar (but with lower vorticity magnitudes) behaviours to that of no SGS model. That is, the shear layer transition starts earlier by weak SGS dissipation that was observed in *a priori* test (figure 6). Therefore, when the grid resolution of *a posteriori* test is the same as that of training data, the grid- and test-filtered inputs with

Re_d	Cases	(N_x, N_y, N_z)	SGS model	L_r/d	$\langle C_{p_b} \rangle$	U_{min}/U	$\langle C_D \rangle$
3900	DNS	(1025, 501, 128)		1.56	−0.87	−0.31	1.00
	LES3900	(449, 271, 64)	G-SR	1.51	−0.90	−0.27	0.94
			G-VG	1.56	−0.88	−0.34	0.96
			T-SR-nFU	0.79	−1.24	−0.21	1.17
			T-VG-nFU	1.28	−0.96	−0.31	1.00
			T-SR-FU	1.59	−0.88	−0.29	0.94
			T-VG-FU	1.56	−0.86	−0.31	0.94
			DSM	1.32	−0.94	−0.31	1.04
			no SGS	1.25	−0.99	−0.23	1.06
	LES3900c	(353, 213, 64)	G-SR	1.16	−1.03	−0.27	1.04
			G-VG	1.07	−1.07	−0.29	1.09
			T-SR-FU	1.55	−0.91	−0.32	0.99
			T-VG-FU	1.49	−0.90	−0.33	0.97
			DSM	0.80	−1.23	−0.18	1.23
			no SGS	0.74	−1.29	−0.20	1.26
	LES3900f	(545, 301, 64)	G-SR	1.22	−0.99	−0.23	0.99
			G-VG	1.39	−0.92	−0.30	0.97
			T-SR-FU	1.62	−0.86	−0.34	0.92
			T-VG-FU	1.57	−0.85	−0.33	0.92
			DSM	1.45	−0.89	−0.32	1.00
			no SGS	1.24	−0.96	−0.31	1.04
5000	DNS	(2049, 1001, 128)		1.39	−0.91	−0.30	1.01
	LES5000	(545, 301, 64)	T-SR-FU	1.45	−0.90	−0.31	0.93
			T-VG-FU	1.47	−0.88	−0.31	0.93
			DSM	1.35	−0.92	−0.31	0.99
			no SGS	1.16	−0.99	−0.32	1.04
10 000	experiment[a]			0.82	−1.13	−0.25	1.14
	LES10000	(1025, 649, 64)	T-SR-FU	0.85	−1.17	−0.27	1.10
			T-VG-FU	0.70	−1.29	−0.25	1.16
			DSM	0.62	−1.36	−0.21	1.25
			no SGS	0.51	−1.47	−0.18	1.31

Table 3. Computational parameters for LESs and simulation results. Here, L_r is the mean recirculation length measured from the base point of the cylinder, $\langle C_{p_b} \rangle$ is the mean base pressure coefficient, U_{min} is the maximum mean negative velocity along the centreline and $\langle C_D \rangle$ is the mean drag coefficient.

[a]Dong *et al.* (2006).

fusion as well as the grid-filtered input alone successfully predict the statistics, while the grid- and test-filtered inputs without fusion do not accurately predict the turbulence statistics. Note that this result is consistent with the *a priori* result of τ_{xy} near the shear layer from T-SR(VG)-nFU. Hence, the grid-filtered input alone is sufficient to produce successful predictions when the trained NN is applied to a *a posteriori* test using the same grids and, thus, additional test-filtered input to the same NN (such as T-SR-nFU and T-VG-nFU) degrades the prediction performance through lower correlations among nodes. On the other hand, when the test-filtered input is provided to a separate NN from that of the grid-filtered input, the combined NNs (such as T-SR-FU and T-VG-FU) avoid this problem and perform quite well.

Note in figure 9 that spurious oscillations appear near the front surface due to the dispersive nature of second-order central difference scheme (CD2). To avoid these oscillations, one should provide much more grids in this laminar accelerating

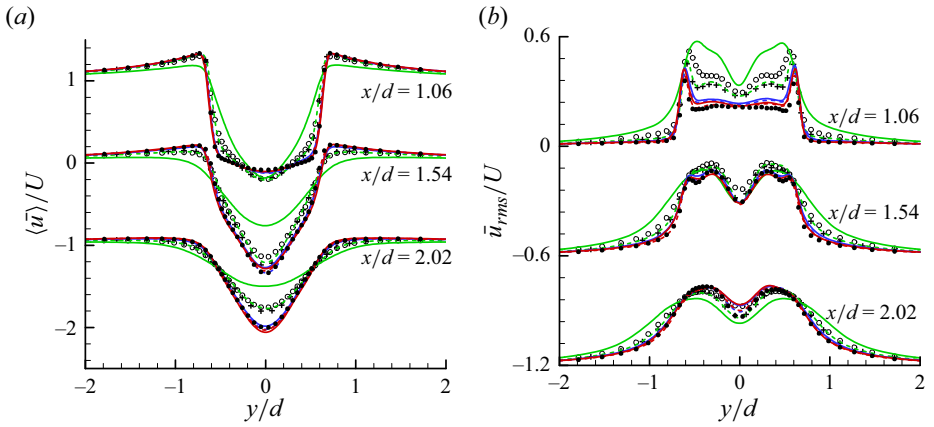

Figure 8. Flow statistics from LES3900 (*a posteriori* test): (*a*) mean streamwise velocity; (*b*) r.m.s. streamwise velocity fluctuations. •, fDNS; —— (blue), G-SR; ---- (blue), G-VG; —— (green), T-SR-nFU; ---- (green), T-VG-nFU; —— (red), T-SR-FU; ---- (red), T-VG-FU; +, DSM; ○, no SGS model.

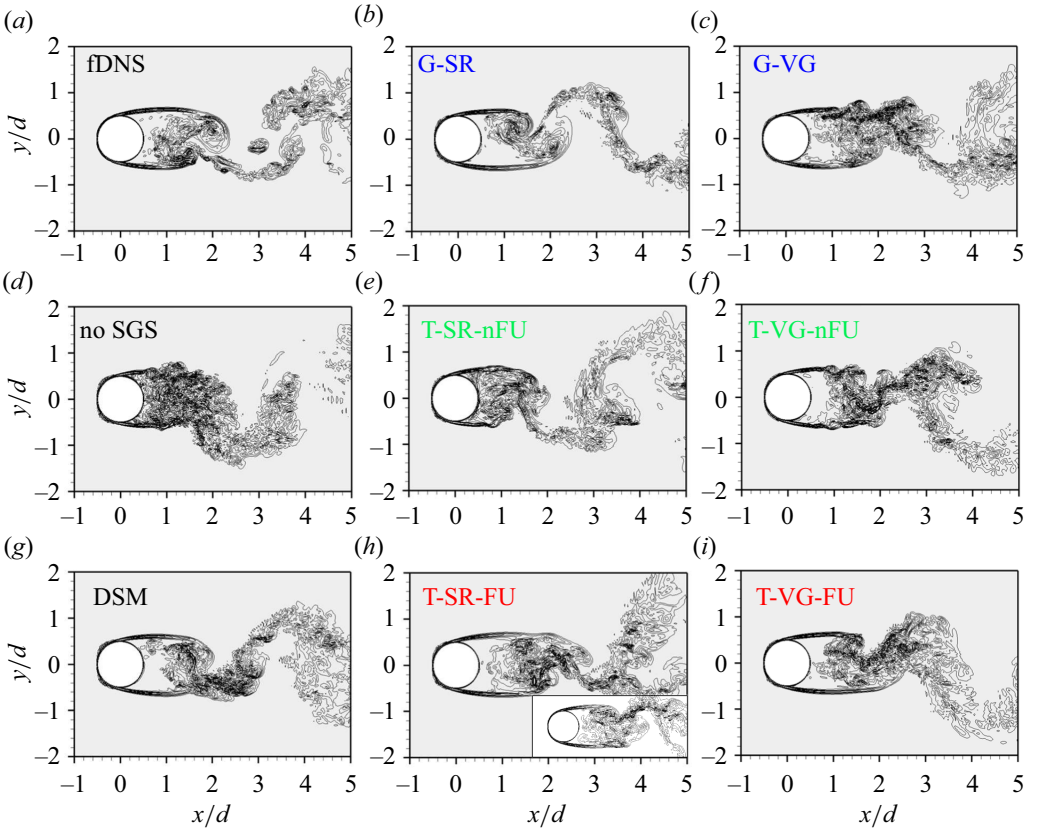

Figure 9. Contours of the instantaneous vorticity magnitude in the near-wake behind the cylinder ($Re_d = 3900$). The contour levels are from $|\omega|d/U = 0$ to 30 by increments of 3. An inset for the case of T-SR-FU is the result of applying a hybrid scheme (QUICK + CD2; Yun *et al.* 2006) to the convection terms of the Navier–Stokes equations.

flow region. To see if these oscillations propagate downstream, a hybrid scheme (QUICK scheme at a laminar accelerating flow region ($x/d < -0.25$) and CD2 elsewhere; Yun, Kim & Choi 2006) is applied to the convection terms for the case of T-SR-FU, and its result is given as an inset in the result of T-SR-FU in figure 9. As shown, the flow structures from CD2 alone and from this hybrid scheme are very similar to each other except for those oscillations, indicating that they do not propagate downstream at this relatively low Reynolds number. However, for a much higher Reynolds number, a hybrid scheme may have to be used to avoid the propagation of these spurious oscillations into downstream.

4.2.2. *LES with a grid resolution different from that of training data ($Re_d = 3900$)*

In this section, we provide results from LES with a grid resolution different from that of training data. Due to the poor performances of T-SR-nFU and T-VG-nFU, other four NN-based SGS models are investigated. Two different grid resolutions (LES3900c and LES3900f) are considered as listed in table 3. LES3900c and LES3900f have coarser and finer grid resolutions on (x, y) planes, respectively, and have the same grid resolution in z direction as that of LES3900 (more on the grid-resolution study is given in Appendix C, and computational costs for estimating the SGS stresses from G-SR and T-SR-FU are compared with that from DSM in Appendix E). For LES3900c, the prediction performances of G-SR and G-VG are significantly degraded especially for the recirculation length and base pressure coefficient. On the other hand, T-SR-FU and T-VG-FU predict these variables quite reasonably, maintaining their prediction capabilities even with coarser grid resolution used. Note that DSM with this coarse resolution predicts much smaller recirculation length, lower base pressure coefficient and higher drag coefficient. For LES3900f, the predictions with DSM are in excellent agreements with those of DNS, but those with G-SR and G-VG become closer to those of DNS but still not better than those with the same grid resolution as that of training data. It is noteworthy that the prediction performances of T-SR-FU and T-VG-FU do not become worse even when the resolution used is different from that of training data.

Figure 10 shows the profiles of the mean streamwise velocity and r.m.s. streamwise velocity fluctuations from four NN-based SGS models with coarser and finer grid resolutions (LES3900c and LES3900f, respectively) than that of training data, together with those of fDNS, DSM and no SGS model. For LES3900c, the use of fusion with grid- and test-filtered input variables (T-SR-FU and T-VG-FU) predicts $\langle\bar{u}\rangle$ and $\bar{u}_{rms}$ quite accurately, whereas the grid-filtered input variables alone (G-SR and G-VG) do not accurately predict them (note, however, that the predictions are still better than those of DSM with this coarser grid resolution). When the grid resolution is finer (LES3900f) than that of training data, both T-SR-FU and T-VG-FU and DSM accurately predict these flow variables, whereas the predictions of G-SR and G-VG are not good. From the results given in table 3 and figure 10, it is clear that the grid- and test-filtered inputs are better than the grid-filtered input alone and fusion connecting these two different filtered inputs significantly increases the prediction performance, when the grid resolution used is different from that of training data. The present results clearly indicate that, by constructing multiple filtered datasets with different filter sizes and using them to train an NN with fusion, one can expect a successful NN-based LES, even if the grid resolution is different from the resolutions used to construct the NN. A similar conclusion was also made in Park & Choi (2021). Note also that this result is consistent with that from the robustness of G-SR and T-SR-FU in § 4.1.

Sirignano *et al.* (2020) evaluated the discretisation errors in LES from finite-difference schemes by comparing finite-differenced spatial derivatives of the filtered velocity on the

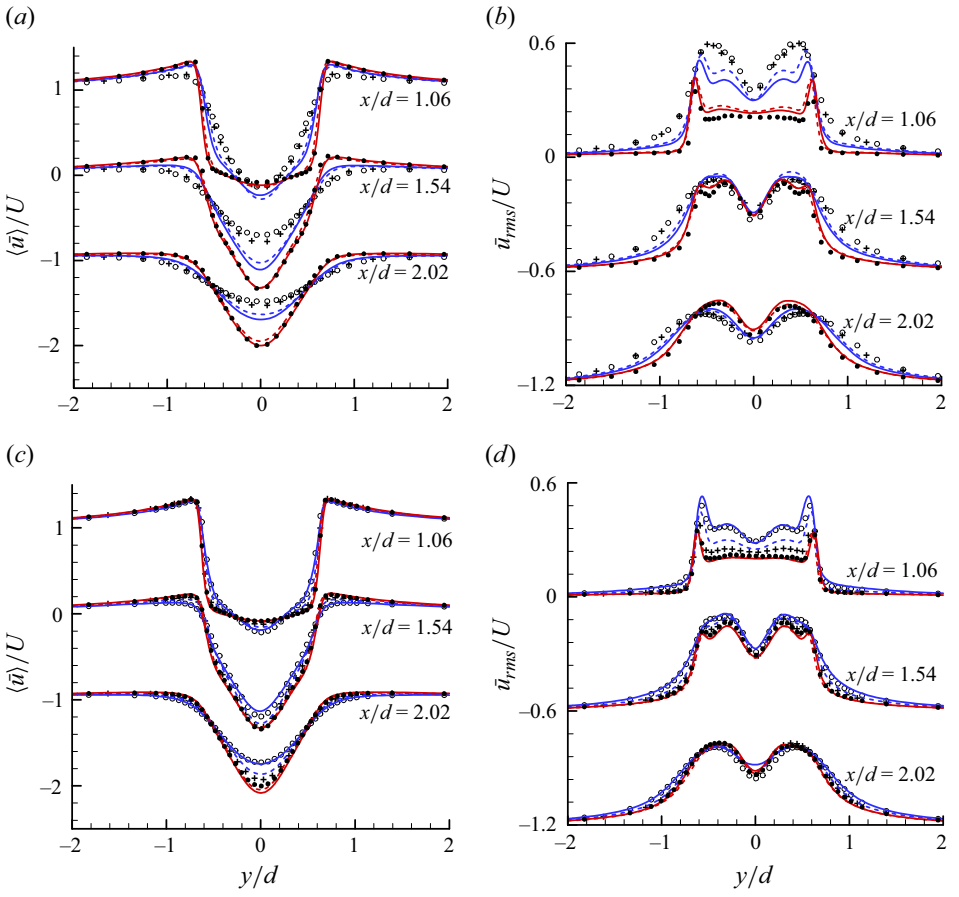

Figure 10. Flow statistics from LES3900c and LES3900f (coarser and finer grid resolutions than that of training data, respectively; *a posteriori* test): (*a*) mean streamwise velocity (LES3900c); (*b*) r.m.s. streamwise velocity fluctuations (LES3900c); (*c*) mean streamwise velocity (LES3900f); (*d*) r.m.s. streamwise velocity fluctuations (LES3900f). •, fDNS; —— (blue), G-SR; ---- (blue), G-VG; —— (red), T-SR-FU; ---- (red), T-VG-FU; +, DSM; ○, no SGS model.

DNS and LES grids, respectively. We follow this approach for estimating the magnitudes of discretisation errors in LES from the second-order finite difference scheme used in the present study, and provide the results in table 4. In this table, $\langle|\delta\bar{\alpha}_{ij}|\rangle/\langle|\bar{\alpha}_{ij}|_{DNS}\rangle$ is the relative magnitude of discretisation error of calculating $\bar{\alpha}_{ij}$ in LES, and $\delta\bar{\alpha}_{ij}$ is obtained as

$$\delta\bar{\alpha}_{ij} = \bar{\alpha}_{ij}|_{LES} - \bar{\alpha}_{ij}|_{DNS}, \tag{4.2}$$

where

$$\left.\begin{aligned} \bar{\alpha}_{ij}|_{LES} &= \frac{\bar{u}_i\left(x_j + \frac{1}{2}\Delta x_j|_{LES}\right) - \bar{u}_i\left(x_j - \frac{1}{2}\Delta x_j|_{LES}\right)}{\Delta x_j|_{LES}}, \\ \bar{\alpha}_{ij}|_{DNS} &= \frac{\bar{u}_i\left(x_j + \frac{1}{2}\Delta x_j|_{DNS}\right) - \bar{u}_i\left(x_j - \frac{1}{2}\Delta x_j|_{DNS}\right)}{\Delta x_j|_{DNS}}, \end{aligned}\right\} \tag{4.3}$$

Cases	(N_x, N_y, N_z)	$\dfrac{\langle\lvert\delta\bar{\alpha}_{ij}\rvert\rangle}{\langle\lvert\bar{\alpha}_{ij}\rvert_{DNS}\rangle}$
LES3900ccc	(225, 137, 64)	0.5690
LES3900cc	(321, 189, 64)	0.5455
LES3900c	(353, 213, 64)	0.5320
LES3900	(449, 271, 64)	0.5136
LES3900f	(545, 301, 64)	0.4986

Table 4. Averaged relative magnitudes of finite-differencing errors, evaluated for filter sizes of $\Delta(\mathrm{LES})/\Delta(\mathrm{DNS}) = 2$ (for $Re_d = 3900$, the size of LES grids in each direction is about two times that of DNS grids; see table 3). The information on LES3900cc (Gcc-64) and LES390ccc (Gccc-64) are given in table 5.

$\langle\cdot\rangle$ is the average in time and over the training zone shown in figure 4(*b*), and $\Delta x_j|_{LES}$ and $\Delta x_j|_{DNS}$ are the grid spacings in LES and DNS, respectively. Table 4 indicates that, for all the cases considered, $\langle|\delta\bar{\alpha}_{ij}|\rangle$ (difference between $\bar{\alpha}_{ij}$ on the DNS and LES grids) is about half the average magnitude of the VG evaluated on the DNS grids, indicating that the finite-difference errors in LES is not so significant, and the NN-based models trained may not suffer form the finite difference errors (see also Sirignano *et al.* (2020) for further discussion).

4.2.3. *LES at higher Reynolds numbers ($Re_d = 5000$ and 10 000)*

In this section, we perform LESs at $Re_d = 5000$ and 10 000, which are higher than that of training data ($Re_d = 3900$). The grid resolutions at $Re_d = 5000$ and 10 000 are the same as and finer than that of LES3900f, respectively, as listed in table 3. These Reynolds numbers are selected as untrained cases, because the flows at these Reynolds numbers are quite different from the trained Reynolds number flow. In the shear layer transition regime ($1000 < Re_d < 200\,000$), the Strouhal number, base pressure coefficient and recirculation length decrease, and the Reynolds stress increases, as the Reynolds number increases (Williamson 1996). These trends can be also observed in table 3. In this regime, with increasing Reynolds number, the onset of shear layer transition occurs earlier, with which the shear-layer vortices evolve earlier and the alternating Kármán vortices exist closer to the base of the cylinder (Dong *et al.* 2006). These flow characteristics can be observed in figure 11, where the instantaneous vortical structures identified by the iso-surfaces of $\lambda_2 = -50U^2/d^2$ (Jeong & Hussain 1995) are shown together with the contours of the instantaneous pressure at $Re_d = 3900$ and 10 000, respectively. Therefore, it will be interesting to see how the NN-based SGS models trained at $Re_d = 3900$ perform at higher Reynolds numbers.

Figure 12 shows the results from T-SR-FU and T-VG-FU at $Re_d = 5000$ (LES5000), together with those of fDNS, DSM and no SGS model. The grid resolution of LES5000 is the same as that of LES3900f. Similar to the results from LES3900f, T-SR-FU, T-VG-FU and DSM have excellent prediction performances. The predicted flow parameters in table 3 are also in good agreements with those of DNS.

Figure 13 shows the profiles of the mean streamwise velocity and r.m.s. streamwise velocity fluctuations from LES10000, together with those of an experiment (Dong *et al.* 2006), DSM and no SGS model. As shown, both T-SR-FU and T-VG-FU accurately predict those statistics (even slightly better than DSM), even though the flow at $Re_d = 10\,000$ is untrained and the transitional phenomena in the separating shear layer is notably altered.

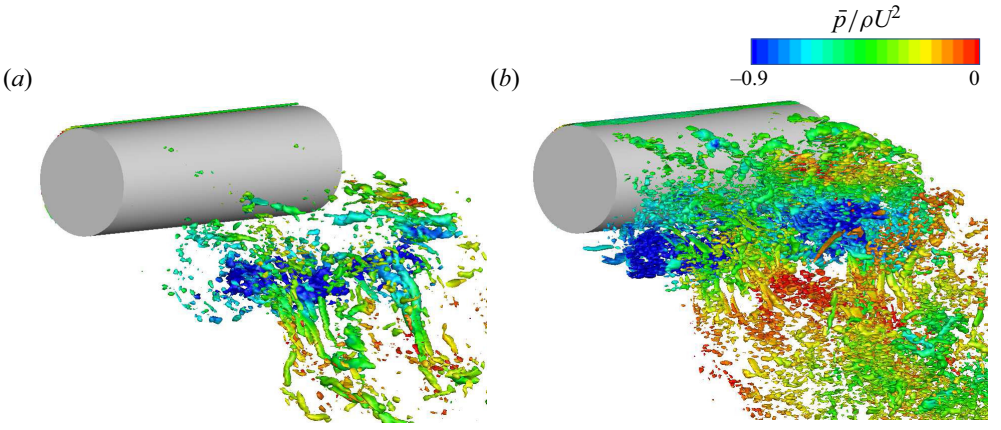

Figure 11. Instantaneous vortical structures coloured with the contours of the instantaneous pressure from T-SR-FU: (*a*) $Re_d = 3900$ (LES3900); (*b*) $Re_d = 10\,000$ (LES10000).

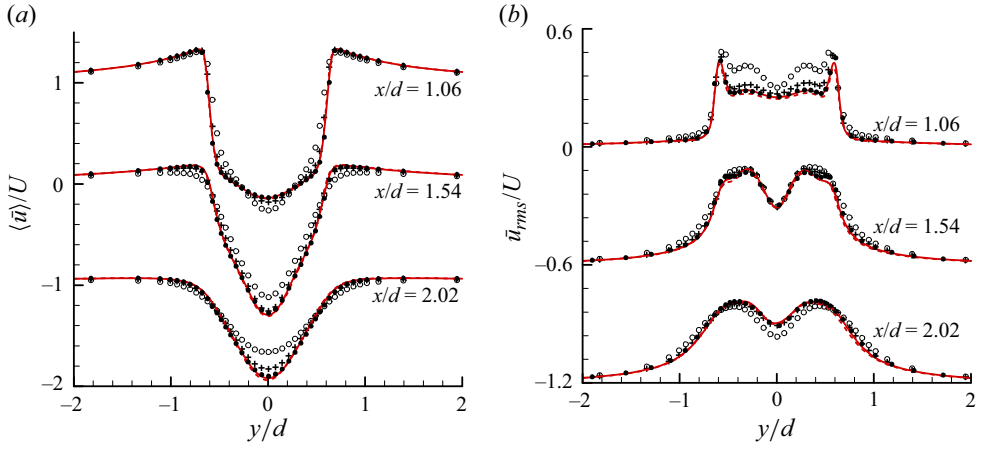

Figure 12. Flow statistics from LES5000 (*a posteriori* test): (*a*) mean streamwise velocity; (*b*) r.m.s. streamwise velocity fluctuations. •, fDNS; —— (red), T-SR-FU; ---- (red), T-VG-FU; +, DSM; ○, no SGS model.

Moreover, T-SR-FU, which uses the SR as the input variable, shows slightly better predictions than T-VG-FU at this Reynolds number. The results provided in this subsection clearly indicate that both the grid- and test-filtered input variables with fusion increase the prediction capability even for untrained Reynolds number flows.

Lastly, one may suggest combining DNS databases at $Re = 3900$ and 5000 to widen input ranges of $\bar{\alpha}_{ij}$ and $\bar{S}_{ij}$ and improve the prediction capability. This approach should work for higher-Reynolds-number flows. Nevertheless, in the present study, we show that the present approach with a database at $Re = 3900$ alone can predict the flows at higher Reynolds numbers.

5. Conclusions

Recently, many studies have been performed to develop NN-based SGS models for LES. However, most of them have focused on simple turbulent flows such as isotropic turbulence

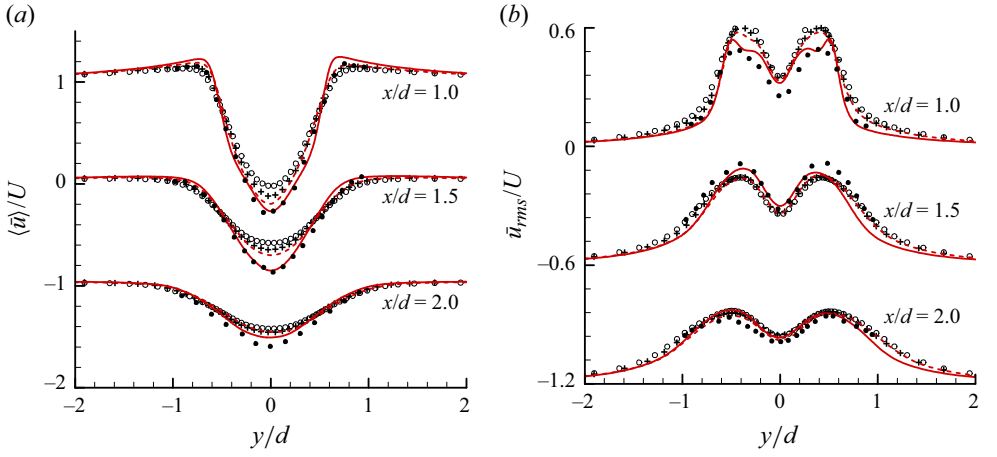

Figure 13. Flow statistics from LES10000 (*a posteriori* test): (*a*) mean streamwise velocity; (*b*) r.m.s. streamwise velocity fluctuations. •, experiment (Dong *et al.* 2006); —— (red), T-SR-FU; ---- (red), T-VG-FU; +, DSM; ○, no SGS model.

and turbulent channel flow, and an application to complex flow is very limited. Since NN-based SGS models should be eventually applied to any complex flows, it is important to develop such models and test them for representative complex flows. Therefore, in the present study, we chose a circular cylinder as a representative complex flow. We believe that the present study may be one of the first attempts to develop and apply NN-based SGS models to a complex flow.

In the present study, FCNNs were constructed to develop SGS models that predicted the SGS stresses for flow over a circular cylinder, and *a priori* and *a posteriori* tests were conducted to estimate their prediction performances. To obtain SGS models, we proposed a new FCNN architecture that used both grid- and test-filtered variables as inputs and fusion connecting these two different inputs, and compared its prediction performance with that of an FCNN architecture that had only the grid-filtered variable as input. As the input variable, the SR or VG tensor at a single grid point was considered. Hence, we constructed six different FCNN-based SGS models: G-SR and G-VG (grid-filtered SR and VG as the input variables, respectively), T-SR-nFU and T-VG-nFU (grid- and test-filtered SR and VG as the input variables, respectively, without fusion) and T-SR-FU and T-VG-FU (grid- and test-filtered SR and VG as the input variables, respectively, with fusion).

For training database, fDNS data were obtained by applying the box filter to the DNS data at $Re_d = 3900$. The training data were extracted from 25 instantaneous fDNS fields during approximately 20 vortex shedding cycles, and the fDNS data from (x, y) planes at four different spanwise locations were used for the training data. The FCNN architectures were trained with these training data to generate six SGS models, and *a priori* and *a posteriori* tests were conducted for the comparison of their prediction performances.

In *a priori* tests, the FCNN-based SGS models had better predictions of the SGS stress, SGS dissipation and backscatter than the DSM. However, the results of T-SR-nFU and T-VG-nFU showed the distributions of SGS shear stress and dissipation opposite to those of fDNS in the shear layer regions near the cylinder, and thus high peaks of backscatter were observed there. Due to the lack of dissipation in these regions, *a posteriori* tests showed early evolution of the shear layer instability and non-physical small-scale vortices in the near-wake region, resulting in inaccurate predictions of turbulence statistics. On the other hand, G-SR, G-VG, T-SR-FU and T-VG-FU showed better performances than

DSM. These four SGS models were applied to LESs with two different grid resolutions which were coarser and finer than that of the training data. With untrained grid resolutions, T-SR-FU and T-VG-FU still showed good prediction performances, but G-SR and G-VG did not, indicating that both the grid- and test-filtered variables with fusion increased the prediction performance when the grid resolution was different from that of the training data. Finally, we applied T-SR-FU and T-VG-FU trained at $Re = 3900$ to LESs at higher Reynolds numbers of $Re_d = 5000$ and 10 000, and also obtained quite accurate turbulence statistics.

Since the present idea of combining the grid- and test-filtered input variables with fusion for constructing an FCNN architecture has not been applied to any simple flow, we apply G-SR and T-SR-FU to LES of turbulent channel flow at $Re_\tau = 178$. As shown in Appendix D, adding the test-filtered variable as an additional input together with fusion increases the prediction accuracy for turbulent channel flow. Therefore, the present FCNN architecture with the grid- and test-filtered input variables and fusion may be applicable to other complex flows.

Lastly, the present NN-based SGS models cannot overcome a well-known limitation of traditional SGS models: inconsistency between *a priori* and *a posteriori* tests. To overcome this inconsistency, Sirignano *et al.* (2020) developed an NN-based SGS model by solving adjoint partial differential equations for isotropic turbulence to match the mean filtered velocity of LES with fDNS data. In addition, Kim *et al.* (2022) developed SGS models based on deep RL for turbulent channel flow to maximise the statistical accuracy such as the mean viscous and Reynolds stresses. In contrast to the isotropic turbulence and turbulent channel flow, it should be very difficult to determine a target to match for flow over/inside a complex geometry because it is *a priori* unknown for those flows. On the other hand, the present NN-based SGS model may have scalability to general flows by accumulating more databases from various turbulent flows and combining those databases into one NN architecture.

Funding. This work is supported by the National Research Foundation through the Ministry of Science and ICT (number 2022R1A2B5B02001586). The computing resources are provided by the KISTI Super Computing Center (number KSC-2021-CRE-0292).

Declaration of interests. The authors report no conflict of interest.

Author ORCIDs.
Haecheon Choi https://orcid.org/0000-0003-0696-847X.

Appendix A. Effects of the size of training data in *a priori* and *a posteriori* tests

At present, the data from 25 instantaneous fDNS fields ($N_t = 25$) during approximately 20 vortex shedding cycles and (x, y) planes at four spanwise locations ($N_s = 4$) per instantaneous field are taken as the training data. Figures 14(a) and 14(b) show the variations of the mean SGS shear stress with the changes in $N_t (= 13, 25$ and $50)$ and $N_s (= 2, 4$ and $8)$, respectively. As shown in this figure, the effect of varying N_t and N_s is very small, indicating that $N_t = 25$ and $N_s = 4$ are sufficient for training purpose.

In addition, in figure 4(b), the domain size for extracting training data is $-1 \leq x/d \leq 6$ and $-1.5 \leq y/d \leq 1.5$. We change this domain size to smaller and larger ones, respectively, and their results are given in figure 15. As shown, the present domain size is sufficient to accurately predict the mean velocity and r.m.s. velocity fluctuations, but the smaller one is too small to carry all the important velocity field information.

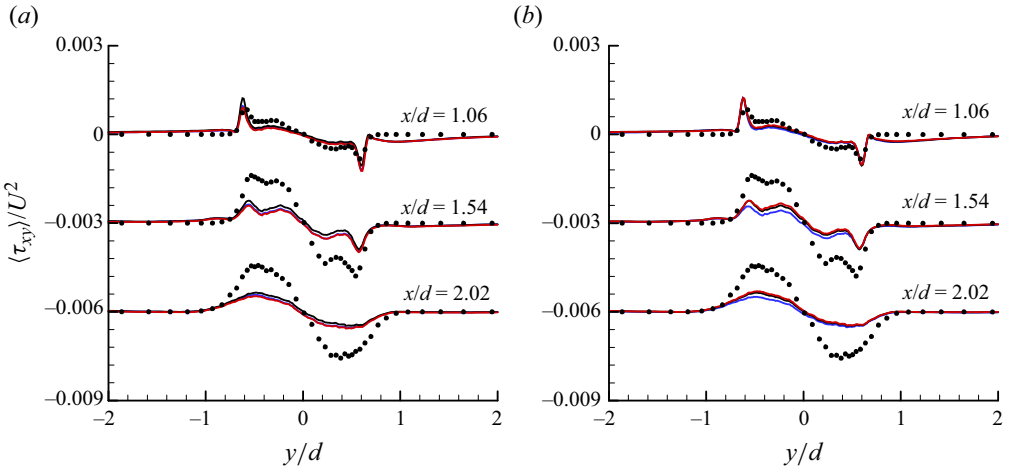

Figure 14. Effect of the number of training data on the mean SGS shear stress (*a priori* test; $Re_d = 3900$): (*a*) $N_t = 25$ (——, black), $N_t = 13$ (——, blue) and $N_t = 50$ (——, red) with $N_s = 4$; (*b*) $N_s = 4$ (——, black), $N_s = 2$ (——, blue) and $N_s = 8$ (——, red) with $N_t = 25$. •, fDNS.

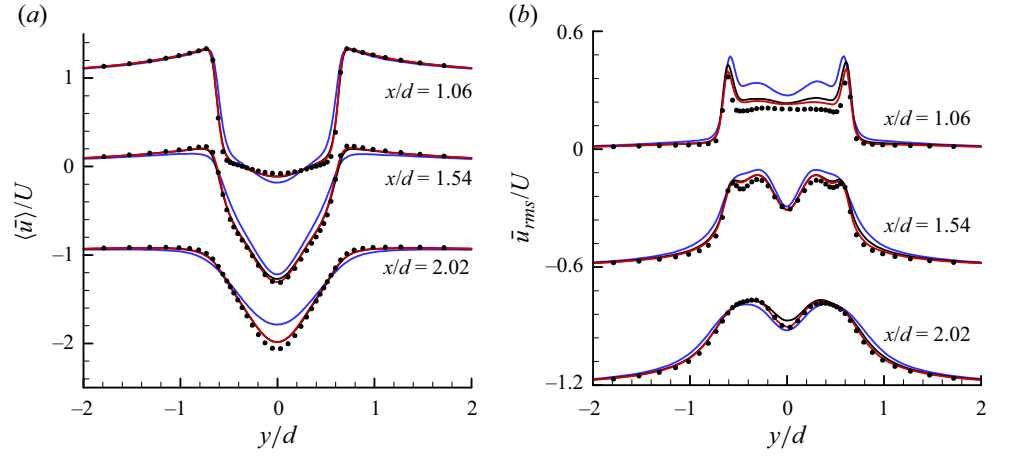

Figure 15. Effect of the domain size of extracting training data on the mean streamwise velocity and r.m.s. streamwise velocity fluctuations (*a posteriori* test; $Re_d = 3900$): (*a*) mean streamwise velocity; (*b*) r.m.s. streamwise velocity fluctuations. •, fDNS; —— (black), present domain ($-1 \le x/d \le 6$, $-1.5 \le y/d \le 1.5$); —— (blue), smaller domain ($-1 \le x/d \le 4$, $-1 \le y/d \le 1$); —— (red), larger domain ($-1 \le x/d \le 8$, $-2 \le y/d \le 2$).

Appendix B. Effects of the numbers of the hidden layers and nodes on the flow statistics from *a posteriori* test

Figure 16 shows the effects of the numbers of the hidden layers (N_{hl}) and nodes (N_{nd}) in G-SR on the mean streamwise velocity and r.m.s. streamwise velocity fluctuations from *a posteriori* test. We test for the cases of $N_{hl} = 1$ to 3 and $N_{nd} = 64$ to 256, respectively. As shown in this figure, one hidden layer ($N_{hl} = 1$) or 64 nodes ($N_{nd} = 64$) are not enough to accurately predict the mean and r.m.s. magnitudes of the streamwise velocity, and at least two hidden layers ($N_{hl} = 2$) and 128 nodes ($N_{nd} = 128$) are required for successful predictions. Larger N_{hl} and N_{nd} do not improve the predictions, as shown in this figure. We also tested the effects of N_{hl} and N_{nd} in T-SR-FU. Again, two hidden layers before fusion

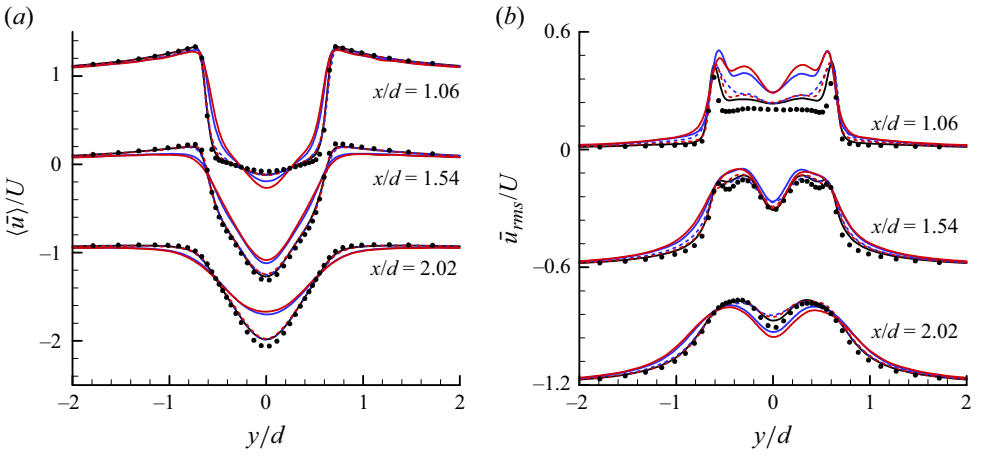

Figure 16. Effects of the numbers of the hidden layers (N_{hl}) and nodes (N_{nd}) in G-SR on the flow statistics (*a posteriori* test; $Re_d = 3900$): (*a*) mean streamwise velocity; (*b*) r.m.s. streamwise velocity fluctuations. •, fDNS; —— (black), $(N_{hl}, N_{nd}) = (2, 128)$; —— (red), $(N_{hl}, N_{nd}) = (1, 128)$; ---- (red), $(N_{hl}, N_{nd}) = (3, 128)$; —— (blue), $(N_{hl}, N_{nd}) = (2, 64)$; ---- (blue), $(N_{hl}, N_{nd}) = (2, 256)$.

and 64 nodes per hidden layer were sufficient for an accurate prediction (not shown in this paper).

Appendix C. Grid-resolution study for *a posteriori* tests at $Re_d = 3900$, 5000 and 10 000

In this appendix, we conduct a grid-resolution study for *a posteriori* test using T-SR-FU at $Re_d = 3900$. The numbers of grid points tested are given in table 5. The case of G-64 uses the grid distribution used for training T-SR-FU (same as that of LES3900), and the cases of G-48 and G-80 use 48 and 80 grid points in z direction, respectively, while maintaining the same grids in x and y directions. The grids of Gf-64 and Gc-64 are the same as those of LES3900f and LES3900c, respectively, and the cases of Gf-80 and Gc-48 use 80 and 48 grid points in z direction, respectively, and the same grid points in x and y directions as those of Gf-64 and Gc-64. Lastly, the cases of Gcc-64 and Gccc-64 use less grid points in x and y directions than those of Gc-64.

The results from nine different grid distributions for $Re_d = 3900$ are shown in figure 17. As shown in this figure, the results from G-48, G-64 and G-80 using T-SR-FU (presented in $y/d \leq 0$) are quite similar among themselves and agree well with those of fDNS, indicating that $N_z = 64$ is sufficient to produce grid-independent results. Note, however, that the results from DSM (G-64) show non-negligible deviations from those of fDNS. With coarser resolution in x and y directions denoted as Gc-64 (presented in $y/d \geq 0$), DSM (Gc-64) provides quite different solutions from those of fDNS (Gc-64), but the solutions of T-SR-FU are quite accurate. Additional decrease in the spanwise resolution does not noticeably degrade the solution from T-SR-FU (Gc-48). With finer resolutions in x and y directions (Gf-64) and in z direction (Gf-80), the solutions of T-SR-FU and DSM agree well with those of fDNS (Gf-64). LESs using T-SR-FU with even coarser grids (Gcc-64 and Gccc-64) diverge (LESs with DSM and no SGS also diverge with these grids), but provide solutions when the SGS stresses are clipped to be zero wherever backscatter occurs, as done in previous studies (Zhou *et al.* 2019; Park & Choi 2021).

Cases	(N_x, N_y, N_z)
G-64 (trained)	(449, 271, 64)
G-48	(449, 271, 48)
G-80	(449, 271, 80)
Gf-64	(545, 301, 64)
Gf-80	(545, 301, 80)
Gc-64	(353, 213, 64)
Gc-48	(353, 213, 48)
Gcc-64	(321, 189, 64)
Gccc-64	(225, 137, 64)

Table 5. Numbers of grid points used for *a posteriori* test at $Re_d = 3900$. Note that the grid distributions of G-64, Gf-64 and Gc-64 in this table are the same as those of LES3900, LES3900f and LES3900c in table 3, respectively.

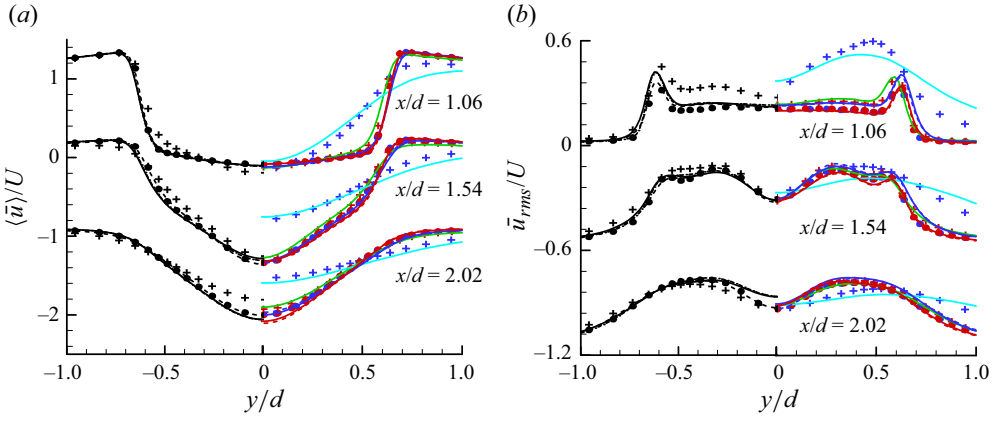

Figure 17. Turbulence statistics in the wake from different grid distributions ($Re_d = 3900$): (*a*) mean streamwise velocity; (*b*) r.m.s. streamwise velocity fluctuations. Here, the results for (G-**) are plotted at $y/d \leq 0$, and those for (Gc-**) and (Gf-**) are plotted at $y/d \geq 0$. • (black), fDNS (G-64); • (blue), fDNS (Gc-64); • (red), fDNS (Gf-64); —— (black), T-SR-FU (G-64); ---- (black), T-SR-FU (G-48); - · - · - · (black), T-SR-FU (G-80); —— (blue), T-SR-FU (Gc-64); —— (green), T-SR-FU (Gcc-64, with *ad hoc* clipping); —— (cyan), T-SR-FU (Gccc-64, with *ad hoc* clipping); ---- (blue), T-SR-FU (Gc-48); —— (red), T-SR-FU (Gf-64); ---- (red), T-SR-FU (Gf-80); + (black), DSM (G-64); + (blue), DSM (Gc-64); + (red), DSM (Gf-64). LESs with Gcc-64 and Gccc-64 without *ad hoc* clipping diverged.

The solution from Gcc-64 with *ad hoc* clipping is quite similar to that from Gc-64, whereas that from Gccc-64 is not good.

In addition, coarser grid resolutions than LES5000 and LES10000 (table 3) are tested at $Re_d = 5000$ and 10 000, respectively. The grid distribution of LES5000 is the same as that of Gf-64, and we further reduce the resolution to G-64 and Gc-64 for $Re_d = 5000$. For $Re_d = 10\,000$, we start from LES10000 and reduce the resolution to Gf-64 and G-64, respectively. The results with these coarser grid resolutions are shown in figure 18. As shown, the predictions from G-64 and Gc-64 for $Re_d = 5000$ and from Gf-64 and G-64 for $Re_d = 10\,000$ are not as good as those from LES5000 and LES10000, respectively, indicating that the present grid distributions of LES5000 and LES10000 are marginal in accurately predicting the second-order statistics at these Reynolds numbers.

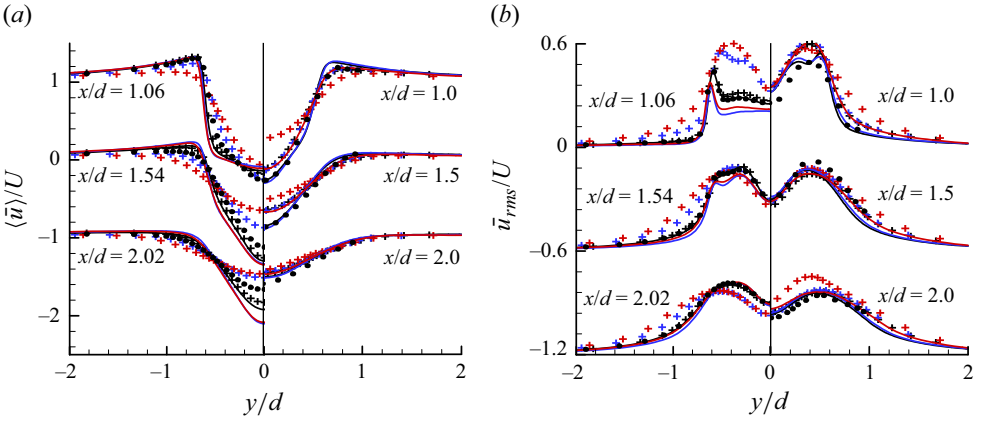

Figure 18. Turbulence statistics in the wake from coarser grids ($Re_d = 5000$ and 10000): (*a*) mean streamwise velocity; (*b*) r.m.s. streamwise velocity fluctuations. Here, the results for $Re_d = 5000$ and 10000 are plotted in $y/d \leq 0$ and $y/d \geq 0$, respectively. •, fDNS (LES5000 (= Gf-64) and LES10000); —— (black), T-SR-FU (LES5000 (= Gf-64) and LES10000); —— (blue), T-SR-FU (G-64 for $Re_d = 5000$ and Gf-64 for $Re_d = 10000$); —— (red), T-SR-FU (Gc-64 for $Re_d = 5000$ and G-64 for $Re_d = 10000$); + (black), DSM (LES5000 (= Gf-64) and LES10000). + (blue), DSM (G-64 for $Re_d = 5000$ and Gf-64 for $Re_d = 10000$); + (red), DSM (Gc-64 for $Re_d = 5000$ and G-64 for $Re_d = 10000$).

Appendix D. LES of turbulent channel flow with grid- and test-filtered inputs and fusion

In this appendix, we train an FCNN for turbulent channel flow with the grid- and test-filtered SR tensors in wall units as the input and fusion. The Reynolds number considered is $Re_\tau = u_\tau \delta/\nu = 178$, where u_τ is the wall-shear velocity and δ is the channel half height. The domain size and number of grid points for DNS are $2\pi\delta \times 2\delta \times \pi\delta$ and $96 \times 97 \times 96$ in the streamwise (x), wall-normal (y) and spanwise (z) directions, respectively. The training data are obtained for the grids of $16 \times 97 \times 16$ by filtering the DNS data. Numerical details are the same as those in Park & Choi (2021).

LESs are performed at $Re_\tau = 178$ for two different SGS models (G-SR and T-SR-FU) with the grid resolutions same ($16 \times 49 \times 16$; LES178) as and coarser ($12 \times 49 \times 12$; LES178c) than that of training data ($16 \times 49 \times 16$). Park & Choi (2021) showed that an FCNN-based SGS model (i.e. G-SR) does not perform well when the grid resolution in wall units is different from that of training data, and this limitation is overcome by training an FCNN with the datasets having two filters whose sizes are bigger and smaller than the grid size in LES. This strategy is quite similar to the idea of T-SR-FU suggested in the present study, in that T-SR-FU is trained with a test-filtered flow variable as well as the grid-filtered one. Hence, we compare the result from LES (LES178c) using G-SR trained with two separate fDNS datasets of $16 \times 49 \times 16$ and $8 \times 49 \times 8$ with that of T-SR-FU.

Figure 19 shows the mean velocity and Reynolds stresses of turbulent channel flow at $Re_\tau = 178$ from two different SGS models (G-SR and T-SR-FU) with the grid resolutions same ($16 \times 49 \times 16$) as and coarser ($12 \times 49 \times 12$) than that of training data ($16 \times 49 \times 16$). With the same grid resolution (LES178), the predictions from T-SR-FU and G-SR are very similar to each other and agree well with fDNS data. With a coarser grid resolution (LES178c), the prediction of G-SR is not accurate and is similar to those of DSM. On the other hand, T-SR-FU predicts better than G-SR and DSM, and the predicted flow variables are very similar to those of G-SR trained with two different fDNS datasets suggested by Park & Choi (2021). Therefore, the FCNN architecture with the grid- and test-filtered

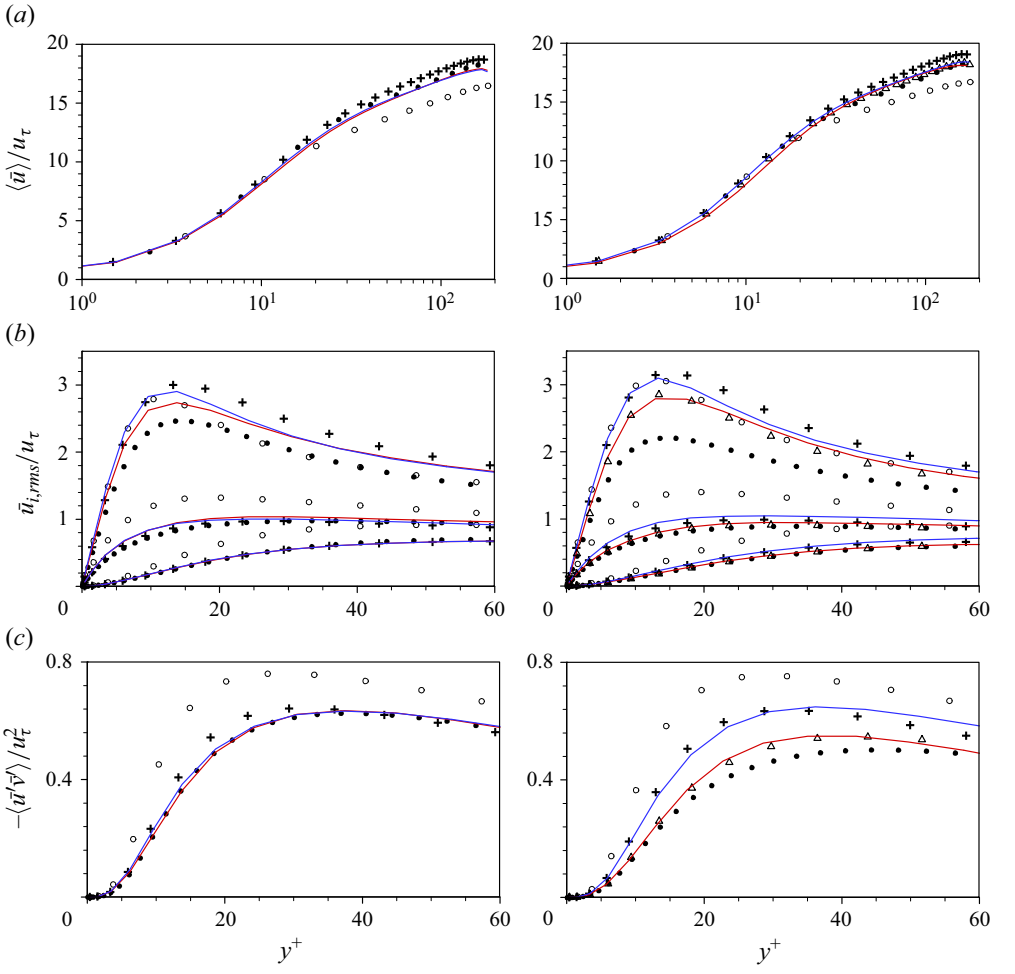

Figure 19. LESs of turbulent channel flow at $Re_\tau = 178$ with grids of $16 \times 49 \times 16$ (LES178, left) and $12 \times 49 \times 12$ (LES178c, right): (*a*) mean streamwise velocity; (*b*) r.m.s. velocity fluctuations; (*c*) Reynolds shear stress. The training data (fDNS) have the grids of $16 \times 49 \times 16$ from DNS with $96 \times 97 \times 96$. •, fDNS; —— (blue), G-SR; —— (red), T-SR-FU; +, DSM; ○, no SGS model. In the right column of this figure, the results from LES ($12 \times 49 \times 12$) using G-SR trained with two datasets of fDNS data ($16 \times 49 \times 16$ and $8 \times 49 \times 8$, respectively) are given with △ (Park & Choi 2021). Here, $\langle\cdot\rangle$ denotes the averaging over the streamwise and spanwise directions and in time.

inputs and fusion performs well for turbulent channel flow, as it worked well for flow over a circular cylinder.

Appendix E. Computational cost

The amounts of CPU time required for estimating the SGS stresses and advancing one computational timestep for NNs (G-SR and T-SR-FU) and DSM are given in table 6. All simulations are performed using 18 CPU cores (Inter(R) Core(TM) i9-9980X CPU @ 3.00 GHz), and the amounts of CPU time are obtained by averaging over 10 computational timesteps. With the same grid resolution (LES3900), the amounts of CPU time required for obtaining the SGS stresses by G-SR and T-SR-FU are approximately 10 and 6.5 times that

(number of grid points)	Model	LES3900c (4.81 million)	LES3900 (7.79 million)	LES3900f (10.50 million)
SGS stresses	DSM	0.177	0.319	0.455
	G-SR	2.099	3.338	4.571
	T-SR-FU	1.278	2.087	2.859
One computational timestep	DSM	1.077	1.998	2.986
	G-SR	2.973	4.953	6.999
	T-SR-FU	2.113	3.761	5.416

Table 6. Amounts of CPU time (seconds) required for estimating the SGS stresses and advancing one computational timestep, respectively.

by DSM, respectively, whereas those required for advancing one computational timestep by G-SR and T-SR-FU are about 2.5 and 2 times that by DSM, respectively. Therefore, NN-based SGS models are slower in terms of CPU time than DSM, when the same grid resolution is taken.

However, as shown in figure 10, the results from LES3900c (coarser resolution) with T-SR-FU are very similar to those from LES3900f (finer resolution) with DSM, indicating that one may reduce the number of grid points with T-SR-FU while keeping the same accuracy (note that the number of grid points of LES3900f is about twice that of LES3900c). The amount of CPU time for LES3900f with DSM is 2.986 seconds for advancing one computational timestep, but it is 2.113 seconds for LES3900c with T-SR-FU. This result suggests that the present NNs may not significantly increase overall CPU time by providing better accuracy with fewer grid points.

References

Akhavan, R., Ansari, A., Kang, S. & Mangiavacchi, N. 2000 Subgrid-scale interactions in a numerically simulated planar turbulent jet and implications for modelling. *J. Fluid Mech.* **408**, 83–120.

Aljure, D.E., Lehmkhul, O., Rodríguez, I. & Oliva, A. 2017 Three dimensionality in the wake of the flow around a circular cylinder at Reynolds number 5000. *Comput. Fluids* **147**, 102–118.

Bardina, J., Ferziger, J. & Reynolds, W.C. 1980 Improved subgrid-scale models for large-eddy simulation. In *13th Fluid and Plasmadynamics Conference*, p. 1357. AIAA.

Beaudan, P. & Moin, P. 1994 Numerical experiments on the flow past a cylinder at sub-critical Reynolds number. *Rep. No. TF* 62. Department of Mechanical Engineering, Stanford University, Stanford, CA, USA.

Beck, A., Flad, D. & Munz, C.D. 2019 Deep neural networks for data-driven LES closure models. *J. Comput. Phys.* **398**, 108910.

Breuer, M. 1998 Numerical and modeling influences on large eddy simulations for the flow past a circular cylinder. *Intl J. Heat Fluid Flow* **19** (5), 512–521.

Burton, G.C. & Dahm, W.J. 2005 Multifractal subgrid-scale modeling for large-eddy simulation. I. Model development and a priori testing. *Phys. Fluids* **17** (7), 075111.

Clark, R.A., Ferziger, J.H. & Reynolds, W.C. 1979 Evaluation of subgrid-scale models using an accurately simulated turbulent flow. *J. Fluid Mech.* **91** (1), 1–16.

Cui, G., Zhou, H., Zhang, Z. & Shao, L. 2004 A new dynamic subgrid eddy viscosity model with application to turbulent channel flow. *Phys. Fluids* **16** (8), 2835–2842.

Domaradzki, J.A. & Saiki, E.M. 1997 A subgrid-scale model based on the estimation of unresolved scales of turbulence. *Phys. Fluids* **9** (7), 2148–2164.

Dong, S., Karniadakis, G.E., Ekmekci, A. & Rockwell, D. 2006 A combined direct numerical simulation-particle image velocimetry study of the turbulent near wake. *J. Fluid Mech.* **569**, 185–207.

Duraisamy, K. 2021 Perspectives on machine learning-augmented Reynolds-averaged and large eddy simulation models of turbulence. *Phys. Rev. Fluids* **6** (5), 050504.

FABRA-BOLUDA, R., FERRI, C., MARTÍNEZ-PLUMED, F. & RAMÍREZ-QUINTANA, M.J. 2022 Robustness testing of machine learning families using instance-level IRT-difficulty. In *Proceedings of the Workshop on AI Evaluation Beyond Metrics (EBeM 2022), Vienna, Austria, 25 July*, vol. 3169.

FERRI, C., HERNÁNDEZ-ORALLO, J. & MODROIU, R. 2009 An experimental comparison of performance measures for classification. *Pattern Recogn. Lett.* **30** (1), 27–38.

FONT, B., WEYMOUTH, G.D., NGUYEN, V.T. & TUTTY, O.R. 2021 Deep learning of the spanwise-averaged Navier–Stokes equations. *J. Comput. Phys.* **434**, 110199.

FRANKE, J. & FRANK, W. 2002 Large eddy simulation of the flow past a circular cylinder at $Re_D = 3900$. *J. Wind Engng Ind. Aerodyn.* **90** (10), 1191–1206.

GAMAHARA, M. & HATTORI, Y. 2017 Searching for turbulence models by artificial neural network. *Phys. Rev. Fluids* **2** (5), 054604.

GERMANO, M., PIOMELLI, U., MOIN, P. & CABOT, W.H. 1991 A dynamic subgrid-scale eddy viscosity model. *Phys. Fluids* **3** (7), 1760–1765.

GHOSAL, S., LUND, T.S., MOIN, P. & AKSELVOLL, K. 1995 A dynamic localization model for large-eddy simulation of turbulent flows. *J. Fluid Mech.* **286**, 229–255.

GLOROT, X. & BENGIO, Y. 2010 Understanding the difficulty of training deep feedforward neural networks. In *Proceedings of the Thirteenth International Conference on Artificial Intelligence and Statistics* (ed. Y.W. Teh & M. Titterington), vol. 9, pp. 249–256. JMLR Workshop and Conference Proceedings.

GUAN, Y., CHATTOPADHYAY, A., SUBEL, A. & HASSANZADEH, P. 2022 Stable *a posteriori* LES of 2D turbulence using convolutional neural networks: backscattering analysis and generalization to higher *Re* via transfer learning. *J. Comput. Phys.* **458**, 111090.

HORIUTI, K. 1997 A new dynamic two-parameter mixed model for large-eddy simulation. *Phys. Fluids* **9** (11), 3443–3464.

IEEE 1990 IEEE standard glossary of software engineering terminology. IEEE Std 610.12-1990, pp. 1–84. IEEE.

IOFFE, S. & SZEGEDY, C. 2015 Batch normalization: accelerating deep network training by reducing internal covariate shift. In *Proceedings of the 32nd International Conference on Machine Learning*, vol. 37, pp. 448–456. JMLR Workshop and Conference Proceedings.

JEONG, J. & HUSSAIN, F. 1995 On the identification of a vortex. *J. Fluid Mech.* **285**, 69–94.

KANG, M., JEON, Y. & YOU, D. 2023 Neural-network-based mixed subgrid-scale model for turbulent flow. *J. Fluid Mech.* **962**, A38.

KARPATHY, A., TODERICI, G., SHETTY, S., LEUNG, T., SUKTHANKAR, R. & FEI-FEI, L. 2014 Large-scale video classification with convolutional neural networks. In *Proceedings of the IEEE Conference on Computer Vision and Pattern Recognition (CVPR)*, pp. 1725–1732. IEEE.

KIM, J., KIM, D. & CHOI, H. 2001 An immersed-boundary finite-volume method for simulations of flow in complex geometries. *J. Comput. Phys.* **171** (1), 132–150.

KIM, J., KIM, H., KIM, J. & LEE, C. 2022 Deep reinforcement learning for large-eddy simulation modeling in wall-bounded turbulence. *Phys. Fluids* **34** (10), 105132.

KRAVCHENKO, A. & MOIN, P. 1998 B-spline methods and zonal grids for numerical simulations of turbulent flows. *Rep. TF*-73. Mechanical Engineering, Stanford University.

KRAVCHENKO, A.G. & MOIN, P. 2000 Numerical studies of flow over a circular cylinder at $Re_D = 3900$. *Phys. Fluids* **12** (2), 403–417.

KURZ, M., OFFENHÄUSER, P. & BECK, A. 2023 Deep reinforcement learning for turbulence modeling in large eddy simulations. *Intl J. Heat Fluid Flow* **99**, 109094.

LANGFORD, J.A. & MOSER, R.D. 1999 Optimal LES formulations for isotropic turbulence. *J. Fluid Mech.* **398**, 321–346.

LANGFORD, J.A. & MOSER, R.D. 2004 Optimal large-eddy simulation results for isotropic turbulence. *J. Fluid Mech.* **521**, 273–294.

LEE, J. 2010 Dynamic global model for large eddy simulation of turbulent flow and scalar transport. PhD thesis, Seoul National University.

LEE, J., CHOI, H. & PARK, N. 2010 Dynamic global model for large eddy simulation of transient flow. *Phys. Fluids* **22** (7), 075106.

LEHMKUHL, O., RODRÍGUEZ, I., BORRELL, R. & OLIVA, A. 2013 Low-frequency unsteadiness in the vortex formation region of a circular cylinder. *Phys. Fluids* **25** (8), 085109.

LI, B., YANG, Z., ZHANG, X., HE, G., DENG, B. & SHEN, L. 2020 Using machine learning to detect the turbulent region in flow past a circular cylinder. *J. Fluid Mech.* **905**, A10.

LILLY, D.K. 1992 A proposed modification of the Germano subgrid-scale closure method. *Phys. Fluids* **4** (3), 633–635.

LIU, B., YU, H., HUANG, H., LIU, N. & LU, X. 2022 Investigation of nonlocal data-driven methods for subgrid-scale stress modeling in large eddy simulation. *AIP Adv.* **12** (6), 065129.
LIU, S., MENEVEAU, C. & KATZ, J. 1994 On the properties of similarity subgrid-scale models as deduced from measurements in a turbulent jet. *J. Fluid Mech.* **275**, 83–119.
LIU, S., MENEVEAU, C. & KATZ, J. 1995 Experimental study of similarity subgrid-scale models of turbulence in the far-field of a jet. *Appl. Sci. Res.* **54**, 177–190.
MA, X., KARAMANOS, G.S. & KARNIADAKIS, G.E. 2000 Dynamics and low-dimensionality of a turbulent near wake. *J. Fluid Mech.* **410**, 29–65.
MACART, J.F., SIRIGNANO, J. & FREUND, J.B. 2021 Embedded training of neural-network subgrid-scale turbulence models. *Phys. Rev. Fluids* **6** (5), 050502.
MANI, A., MOIN, P. & WANG, M. 2009 Computational study of optical distortions by separated shear layers and turbulent wakes. *J. Fluid Mech.* **625**, 273–298.
MITTAL, R. 1995 Large-eddy simulation of flow past a circular cylinder. In *Center for Turbulence Research Annual Research Briefs: 1995*. Stanford University, Stanford, CA, USA.
MITTAL, R. & MOIN, P. 1997 Suitability of upwind-biased finite difference schemes for large-eddy simulation of turbulent flows. *AIAA J.* **35** (8), 1415–1417.
MOSER, R.D., MALAYA, N.P., CHANG, H., ZANDONADE, P.S., VEDULA, P., BHATTACHARYA, A. & HASELBACHER, A. 2009 Theoretically based optimal large-eddy simulation. *Phys. Fluids* **21** (10), 105104.
NAIR, V. & HINTON, G.E. 2010 Rectified linear units improve restricted Boltzmann machines. In *Proceedings of the 27th International Conference on Machine Learning (ICML-10)*, pp. 807–814. Omnipress.
NICOUD, F. & DUCROS, F. 1999 Subgrid-scale stress modelling based on the square of the velocity gradient tensor. *Flow Turbul. Combust.* **62** (3), 183–200.
NICOUD, F., TODA, H.B., CABRIT, O., BOSE, S. & LEE, J. 2011 Using singular values to build a subgrid-scale model for large eddy simulations. *Phys. Fluids* **23** (8), 085106.
NORBERG, C. 1993 Pressure forces on a circular cylinder in cross flow. In *Bluff-Body Wakes, Dynamics and Instabilities* (ed. H. Eckelmann, J.M.R. Graham, P. Huerre & P.A. Monkewitz)*: IUTAM Symposium, Göttingen, Germany September 7–11, 1992*, pp. 275–278. Springer.
NORBERG, C. 1994 An experimental investigation of the flow around a circular cylinder: influence of aspect ratio. *J. Fluid Mech.* **258**, 287–316.
NORBERG, C. 1998 LDV-measurements in the near wake of a circular cylinder. *ASME Paper No. FEDSM98-5208*. ASME.
NOVATI, G., DE LAROUSSILHE, H.L. & KOUMOUTSAKOS, P. 2021 Automating turbulence modelling by multi-agent reinforcement learning. *Natl Mach. Intell.* **3** (1), 87–96.
PAL, A. 2019 Deep learning parameterization of subgrid scales in wall-bounded turbulent flows. arXiv:1905.12765.
PARK, J. & CHOI, H. 2021 Toward neural-network-based large eddy simulation: application to turbulent channel flow. *J. Fluid Mech.* **914**, A16.
PARK, N., LEE, S., LEE, J. & CHOI, H. 2006 A dynamic subgrid-scale eddy viscosity model with a global model coefficient. *Phys. Fluids* **18** (12), 125109.
PARNAUDEAU, P., CARLIER, J., HEITZ, D. & LAMBALLAIS, E. 2008 Experimental and numerical studies of the flow over a circular cylinder at Reynolds number 3900. *Phys. Fluids* **20** (8), 085101.
PAWAR, S., SAN, O., RASHEED, A. & VEDULA, P. 2020 A priori analysis on deep learning of subgrid-scale parameterizations for Kraichnan turbulence. *Theor. Comput. Fluid Dyn.* **34**, 429–455.
PORTÉ-AGEL, F., MENEVEAU, C. & PARLANGE, M.B. 2000 A scale-dependent dynamic model for large-eddy simulation: application to a neutral atmospheric boundary layer. *J. Fluid Mech.* **415**, 261–284.
RASTHOFER, U. & GRAVEMEIER, V. 2013 Multifractal subgrid-scale modeling within a variational multiscale method for large-eddy simulation of turbulent flow. *J. Comput. Phys.* **234**, 79–107.
ROZEMA, W., BAE, H.J., MOIN, P. & VERSTAPPEN, R. 2015 Minimum-dissipation models for large-eddy simulation. *Phys. Fluids* **27** (8), 085107.
SALVETTI, M.V. & BANERJEE, S. 1995 A priori tests of a new dynamic subgrid-scale model for finite-difference large-eddy simulations. *Phys. Fluids* **7** (11), 2831–2847.
SAMIEE, M., AKHAVAN-SAFAEI, A. & ZAYERNOURI, M. 2020 A fractional subgrid-scale model for turbulent flows: theoretical formulation and a priori study. *Phys. Fluids* **32** (5), 055102.
SARGHINI, F., DE FELICE, G. & SANTINI, S. 2003 Neural networks based subgrid scale modeling in large eddy simulations. *Comput. Fluids* **32** (1), 97–108.
SILVIS, M.H., REMMERSWAAL, R.A. & VERSTAPPEN, R. 2017 Physical consistency of subgrid-scale models for large-eddy simulation of incompressible turbulent flows. *Phys. Fluids* **29** (1), 015105.
SIRIGNANO, J., MACART, J.F. & FREUND, J.B. 2020 DPM: a deep learning PDE augmentation method with application to large-eddy simulation. *J. Comput. Phys.* **423**, 109811.

SMAGORINSKY, J. 1963 General circulation experiments with the primitive equations: I. The basic experiment. *Mon. Weath. Rev.* **91** (3), 99–164.

STOFFER, R., VAN LEEUWEN, C.M., PODAREANU, D., CODREANU, V., VEERMAN, M.A., JANSSENS, M., HARTOGENSIS, O.K. & VAN HEERWAARDEN, C.C. 2021 Development of a large-eddy simulation subgrid model based on artificial neural networks: a case study of turbulent channel flow. *Geosci. Model Develop.* **14** (6), 3769–3788.

SUBEL, A., CHATTOPADHYAY, A., GUAN, Y. & HASSANZADEH, P. 2021 Data-driven subgrid-scale modeling of forced burgers turbulence using deep learning with generalization to higher Reynolds numbers via transfer learning. *Phys. Fluids* **33** (3), 031702.

TRIAS, F.X., FOLCH, D., GOROBETS, A. & OLIVA, A. 2015 Building proper invariants for eddy-viscosity subgrid-scale models. *Phys. Fluids* **27** (6), 065103.

VERSTAPPEN, R.W.C.P., BOSE, S., LEE, J., CHOI, H. & MOIN, P. 2010 A dynamic eddy-viscosity model based on the invariants of the rate-of-strain. In *Proceedings of the Summer Program 2010 (Center for Turbulence Research, Stanford University)*, pp. 183–192. Stanford University, Stanford, CA, USA.

VÖLKER, S., MOSER, R.D. & VENUGOPAL, P. 2002 Optimal large eddy simulation of turbulent channel flow based on direct numerical simulation statistical data. *Phys. Fluids* **14** (10), 3675–3691.

VREMAN, A.W. 2004 An eddy-viscosity subgrid-scale model for turbulent shear flow: algebraic theory and applications. *Phys. Fluids* **16** (10), 3670–3681.

VREMAN, B., GEURTS, B. & KUERTEN, H. 1994 On the formulation of the dynamic mixed subgrid-scale model. *Phys. Fluids* **6** (12), 4057–4059.

WANG, Y., YUAN, Z., XIE, C. & WANG, J. 2021 Artificial neural network-based spatial gradient models for large-eddy simulation of turbulence. *AIP Adv.* **11** (5), 055216.

WILLIAMSON, C.H. 1996 Vortex dynamics in the cylinder wake. *Annu. Rev. Fluid Mech.* **28** (1), 447–539.

WOLLBLAD, C. & DAVIDSON, L. 2008 Pod based reconstruction of subgrid stresses for wall bounded flows using neural networks. *Flow Turbul. Combust.* **81**, 77–96.

XIE, C., WANG, J., LI, H., WAN, M. & CHEN, S. 2020*a* Spatially multi-scale artificial neural network model for large eddy simulation of compressible isotropic turbulence. *AIP Adv.* **10** (1), 015044.

XIE, C., WANG, J. & WEINAN, E. 2020*b* Modeling subgrid-scale forces by spatial artificial neural networks in large eddy simulation of turbulence. *Phys. Rev. Fluids* **5** (5), 054606.

XIE, C., YUAN, Z. & WANG, J. 2020*c* Artificial neural network-based nonlinear algebraic models for large eddy simulation of turbulence. *Phys. Fluids* **32** (11), 115101.

YUAN, Z., XIE, C. & WANG, J. 2020 Deconvolutional artificial neural network models for large eddy simulation of turbulence. *Phys. Fluids* **32** (11), 115106.

YUN, G., KIM, D. & CHOI, H. 2006 Vortical structures behind a sphere at subcritical Reynolds numbers. *Phys. Fluids* **18** (1), 015102.

ZANDONADE, P.S., LANGFORD, J.A. & MOSER, R.D. 2004 Finite-volume optimal large-eddy simulation of isotropic turbulence. *Phys. Fluids* **16** (7), 2255–2271.

ZANG, Y., STREET, R.L. & KOSEFF, J.R. 1993 A dynamic mixed subgrid-scale model and its application to turbulent recirculating flows. *Phys. Fluids* **5** (12), 3186–3196.

ZANNA, L. & BOLTON, T. 2020 Data-driven equation discovery of ocean mesoscale closures. *Geophys. Res. Lett.* **47** (17), e2020GL088376.

ZHOU, Z., HE, G., WANG, S. & JIN, G. 2019 Subgrid-scale model for large-eddy simulation of isotropic turbulent flows using an artificial neural network. *Comput. Fluids* **195**, 104319.